Constant Modulus MIMO Radar Waveform Design With Minimum Peak Sidelobe Transmit Beampattern

Wen Fan, Junli Liang, *Senior Member, IEEE*, and Jian Li, *Fellow, IEEE*

***Abstract*—This paper addresses the problem of minimum peak sidelobe transmit beampattern design for colocated multiple-input multiple-output radar systems. Two new methods are proposed to achieve it via designing constant modulus (CM) waveforms directly: One is to maximize the ratio of the minimum mainlobe level to the peak sidelobe level (PSL) without specifying pattern masks, and another is to minimize PSL under the mainlobe ripple and unspecified waveform modulus constraints. The resultant optimization problems are difficult to solve due to the coupled numerator and denominator of the quadratic fractional programming problem formulation in the former and double-sided quadratic constraints and unknown waveform modulus in the latter. For the former, we decouple the numerator and denominator by equivalent transformation and introduction of boundary-type auxiliary variables in order that feasible methods are derived to tackle them independently and efficiently. For the latter, we simplify the coupled double-sided quadratic constraints on the same waveform vector into those on different single auxiliary variables to tackle the corresponding nonconvex optimization problem. Numerical examples show that the proposed algorithms can attain sufficient low peak sidelobe beampattern levels under the CM constraints.**

***Index Terms*—Colocated MIMO radar, waveform design, transmit beampattern, constant modulus, minimum sidelobe, ripple control, quadratic fractional programming (QFP), double-sided quadratic constraints, unimodular quadratic program (UQP).**

I. Introduction

COLOCATED multiple-input multiple-output (MIMO) radar systems have been attracting much more attention during the past decades [1]–[4]. Unlike phased-array radars [5] that transmit scaled versions of a single waveform with different antennas, colocated MIMO radar system has an extra degree of freedom of waveform transmission to exploit waveform diversity [6]. With such an advantage, colocated MIMO radar systems can have the improved parameter identifiability, enhanced spatial resolution, and increased flexibility for transmit beampattern design [1], [3], [6], [7]. Waveform design plays an important role in colocated MIMO radar systems.

Generally, the colocated MIMO radar waveform design problem can be classified into two categories. One is to design transmit waveforms and receive filters jointly to achieve the maximum output signal-to-interference-plus-noise ratio [8], [9], which can enhance the target detection performance and suppress signal-dependent interferences. Another is to design MIMO radar waveforms with desirable transmit beampattern to control the radiation power distribution.

For the second category, it is also classified into two subclasses. *One possible solution* is to apply the two-step strategy to design the MIMO radar waveforms with desirable transmit beampattern. Firstly, the transmit beampattern is realized through the choice of a waveform covariance matrix [2], [6], [10]–[13]. Then, the transmitted waveforms are derived from the obtained covariance matrix [6], [14], [15].

Since the MIMO radar transmit beampattern is closely related to the covariance matrix of the transmitted waveforms, [6] and [16] propose several beampattern design metrics to match or approximate a desired transmit beampattern via optimizing the waveform covariance matrix. A penalty term, i.e., a cross-correlation term of signals reflected back to the radar system from targets, is added to the aforementioned matching metric to improve the parameter estimation accuracy and resolution of the MIMO radar system [2]. In addition, [2] formulates the minimum sidelobe beampattern design problem via maximizing the difference between the synthesized beampattern levels in the mainlobe region and those in the sidelobe region.

In addition to the peak sidelobe level (PSL), another metric, i.e., the mainlobe ripple term, is also considered in practical applications to improve the robustness of radar system, especially when the direction of target is imprecisely known. The direct or indirect control of mainlobe ripple methods are proposed in [12] via choosing a positive definite matrix, and the relationship between the MIMO radar transmit beampattern design and conventional finite-impulse-response filter design is derived to obtain the desirable beampattern with the least system cost. In order to reduce the computation burden, [10] derives an unconstrained transmit beampattern algorithm and [11] utilizes the fast Fourier transform.

In recent years, robust approaches to transmit beampattern design are also brought into focus. In [17], the uncertainties of the steering vectors in the sidelobe region and mainlobe region are introduced into the design problem. Additionally, [18] derives a general framework for the robust beampattern design.

Manuscript received December 11, 2017; revised May 7, 2018; accepted June 8, 2018. Date of publication June 18, 2018; date of current version July 2, 2018. The associate editor coordinating the review of this manuscript and approving it for publication was Dr. Fabiola Colone. This work was supported in part by the Natural Science Foundation of China under Grant 61471295, in part by the Aeronautical Science Foundation of China under Grant 20172053017, and in part by the Central University Funds under Grants G2016KY0308, G2016KY0002, and 17GH030144, and in part by the Key Research Program of Frontier Sciences, CAS under Grant QYZDY-SSW-JSC035. *(Corresponding author: Junli Liang.)*

W. Fan and J. Liang are with the School of Electronics and Information, Northwestern Polytechnical University, Xi'an 710072, China (e-mail: fanwen@mail.nwpu.edu.cn; liangjunli@nwpu.edu.cn).

J. Li is with the Department of Electronic Engineering and Information Science, University of Science and Technology of China, Hefei 230000, China (e-mail: li@dsp.ufl.edu).

Color versions of one or more of the figures in this paper are available online at http://ieeexplore.ieee.org.

Digital Object Identifier 10.1109/TSP.2018.2847636

Other MIMO radar transmit beampattern design methods are given in, e.g., [13], [19]–[22], and the references therein.

Once the covariance matrix is obtained via solving the aforementioned problems, the remaining task is to synthesize transmit waveforms under practical constraints from the covariance matrix, such as constant modulus (CM) or peak-to-average-power ratio constraints [23]–[25]. [6] uses binary-shift keying coded waveforms while [14] utilizes a cyclic algorithm (CA) to synthesize the CM waveforms. Other related literatures include [13], [15].

However, the aforementioned two-step methods exist approximation errors, especially for the applications of sidelobe suppression, ripple control, and deep null, etc [14].

Another solution is to design transmit waveforms directly to achieve the desired transmit beampattern. In [26], the direct waveform design problem is formulated as a semidefinite relaxation programming problem. In [27], a successive closed-form technique is proposed to design CM waveforms. Additionally, [28] applies the alternating direction method of multipliers to achieve desired beampattern. However, these direct designs only focus on minimizing the mean squared error between the synthesized beampattern and the desired beampattern, and pay little attention to PSL suppression and mainlobe ripple constraints of the transmit beampattern.

Unlike them, we will impose more restrictions on the sidelobe and the mainlobe regions of the transmit beampattern. Under the CM constraints, we propose two new design metrics to achieve minimum peak sidelobe transmit beampattern (MPSTB) via designing waveforms directly.

On the other hand, the alternating direction method of multipliers (ADMM) [29] has been exhibiting great performance in a number of nonconvex problems [30]–[33], just name a few. To this end, we are inspired to develop ADMM-based algorithms for the proposed design metrics such that nonconvex problems can be tackled. In addition, it is shown that the proposed algorithms can converge to optimal solutions under some mild conditions [30]. It is worth highlighting several aspects of the proposed approaches here:

1) Under the CM constraints, it is difficult to provide both feasible beampattern design masks and reasonable (pattern) power reference points in the mainlobe region due to the resultant freedom degree loss on the designed waveforms. For this reason, we maximize the ratio of the minimum mainlobe level (MML) to the PSL without specifying pattern masks to achieve the MPSTB, which results in a quadratic fractional programming (QFP) problem [34];
2) It is difficult to solve such a QFP problem since both the numerator and denominator are the functions of the waveform variables to optimize. We first introduce boundary-type auxiliary variables to decouple the numerator and denominator, and then derive a feasible method to tackle them independently and efficiently;
3) In some practical applications, the target direction is imprecisely known and mainlobe with flat radiation power is desirable for robust target detection. For this reason, we consider controlling the mainlobe ripple and suppressing the PSL simultaneously. Thus, another design metric based on the mainlobe ripple constraints is proposed for the MPSTB design. In addition, unlike [2] and [12], we do not introduce a scale factor (see Eq. (9) of [2] for details) or relax the elemental power constraint (see Eqs. (16)–(17) of [12] for details) for the beampattern mask but consider the waveform modulus as an unknown constant. In such a problem formulation, we can precisely control the beampattern levels in the interested angle regions comparing to the two-step strategy proposed in [12];
4) To solve such an optimization problem with the coupled double-sided quadratic constraints (mainlobe ripple constraints) [35], we simplify the coupled constraints on the same waveform vector into those on different single auxiliary variable vectors. Thus, each formed subproblem can be solved efficiently;
5) Especially, the subproblem with CM constraints (also known as unimodular quadratic program (UQP) [36], [37]) is efficiently solved by introducing phase-type auxiliary variables. In addition, the theoretical analysis is also given to show that the proposed algorithms can converge to the set of stationary solutions, if the step size (penalty parameter) is chosen large enough [32], [33].

The rest of this paper is organized as follows. The problems of interest are formulated in Section II. The solutions to the two optimization problems are given in Section III. Numerical examples are presented in Section IV. Conclusions are drawn in Section V.

Notation: Matrices and vectors are denoted by boldface uppercase and lowercase, respectively. $\|\cdot\|$ denotes the Euclidean norm of a vector and $\|\cdot\|_F$ denotes the Frobenius norm. For a complex vector $\mathbf{x}$, we use $x(\bar{n})$, $|x(\bar{n})|$, and $\angle x(\bar{n})$ to denote the $\bar{n}$th element of $\mathbf{x}$, and its corresponding modulus and phase. $\mathbf{I}_N$ denotes the $N\times N$-dimensional identity matrix. The transpose and conjugate transpose of a matrix or vector are denoted by $(\cdot)^T$ and $(\cdot)^H$, respectively, while $\otimes$ denotes the Kronecker matrix product, $\{\cdot\}$ denotes the variable set, and std$(\cdot)$ denotes the standard deviation. Re$\langle\cdot,\cdot\rangle$ denotes real part of the inner product of vectors. The symbols $\mathbb{C}$ and $\mathbb{R}$ are, respectively, the complex and real space.

II. Problem Formulation and Design Metrics

In this section, we first review the transmit beampattern design for colocated MIMO radar systems. Then we formulate two new design metrics to achieve MPSTB.

A. Problem Formulation

Consider a colocated MIMO radar system composed of L transmit antennas. Let $x_l(n), n = 1, ..., N$, denote the discrete time radar waveform radiated by the lth antenna, for $l = 1, ..., L$, where N denotes the number of samples of each radar waveform. Then, under the assumption that the propagation is nondispersive and that the transmitted probing signals are narrowband, the base-band signal at the angular location θ can be expressed as [2], [6]

$$\sum_{l=1}^{L} e^{-j2\pi f_0 \tau_l(\theta)} x_l(n) \triangleq \mathbf{a}^H(\theta)\mathbf{x}(n),\ n = 1, \cdots, N, \quad (1)$$

where $j = \sqrt{-1}$, f_0 is the carrier frequency, $\tau_l(\theta) = \frac{(l-1)\bar{d}\sin(\theta)}{\bar{v}}$, $\bar{d}$ is the inter-element spacing between two adjacent

transmit antennas, $\bar{v}$ denotes the speed of propagation,

$$\mathbf{x}(n) = [x_1(n), x_2(n), \cdots, x_L(n)]^T \in \mathbb{C}^{L\times 1}, \tag{2}$$

and

$$\mathbf{a}(\theta) = [e^{j2\pi f_0 \tau_1(\theta)}, e^{j2\pi f_0 \tau_2(\theta)}, \cdots, e^{j2\pi f_0 \tau_L(\theta)}]^T \in \mathbb{C}^{L\times 1}. \tag{3}$$

Under the assumption that the transmit antenna of the MIMO radar system is calibrated, that is, $\mathbf{a}(\theta)$ is a known function of θ, the transmit pattern of the transmitted signal at the location θ is given by [2]

$$\begin{aligned} P(\theta) &= \mathbf{a}(\theta)\sum_{n=1}^{N}\mathbf{x}^H(n)\mathbf{x}(n)\mathbf{a}^H(\theta) \\ &= \mathbf{x}^H\mathbf{A}(\theta)\mathbf{A}^H(\theta)\mathbf{x}, \end{aligned} \tag{4}$$

where $\mathbf{A}(\theta) = \mathbf{I}_N \otimes \mathbf{a}(\theta) \in \mathbb{C}^{LN\times N}$, $\mathbf{x} = [\mathbf{x}^T(1), \mathbf{x}^T(2), \cdots, \mathbf{x}^T(N)]^T \in \mathbb{C}^{LN\times 1}$.

Usually, the beampattern design problem is to synthesize radar waveforms $\mathbf{x}$ (waveform set) under the CM constraints [23]–[25], [38], [39]

$$|x(\bar{n})| = \xi,\ \bar{n} = 1, \cdots, NL, \tag{5}$$

where $\xi > 0$ is the modulus of the waveform vector $\mathbf{x}$.

The task of MIMO transmit beampattern design is to synthesize CM radar waveform vector $\mathbf{x}$ in order that at the specified angular locations the desired beampattern levels are formed.

B. MPSTB Design Metrics for Colocated MIMO Radar System

The low PSL is desirable to reduce radar clutter/jammer vulnerability, and the mainlobe with flat radiation power is desirability of robust radar detection [2], [3], [12]. The minimum PSL and mainlobe ripple control transmit beampattern design problems have been addressed in [2] and [12], respectively. However, these methods do not design transmit waveforms directly but adopt an indirect two-step strategy. In addition, the power levels of the transmit beampattern are governed by the power assigned to the waveforms [2], [12]. Hence, waveforms with CM constraints imply that unlike the MPSTB design in phased-array radars [40], it is not easy to provide reasonable (pattern) power reference point (or beampattern masks) in the mainlobe region for colocated MIMO radar systems and thus we cannot minimize the PSL in the objective function directly.

In this subsection, we propose two new design metrics to synthesize CM waveform vector $\mathbf{x}$ directly: i) differing from [2], we take the MML and the PSL as merits, and maximize the ratio of the MML to the PSL without specifying pattern masks to suppress the PSL and also enhance the mainlobe level; ii) for ripple constraints (with a given beampattern mask), in [12], the elemental power constraint (see Eqs. (16)–(17) of [12] for details) is relaxed to make the design problem feasible. Differing from [12], we show that the waveform modulus ξ (elemental power constraint) is related to the scaling factor, and we set ξ as an unknown parameter to be optimized. Thus, the design metric based on the mainlobe ripple constraints is formulated.

For the sake of discussion, the angle regions are divided into three discrete grid sets, Θ, Ω, and Φ, namely, mainlobe, sidelobe, and transition bands, respectively. Among them the mainlobe and sidelobe sets are composed of M and S angle grids, respectively, i.e., $\Theta = \{\theta_m\}_{m=1}^{M}$ and $\Omega = \{\vartheta_s\}_{s=1}^{S}$.

1) Without Beampattern Mask Design (WBM-Design): In the first problem formulation, we consider designing the MPSTB without pattern masks, i.e.,

$$\begin{aligned} \max_{\mathbf{x}}\ & \frac{\min_{\theta_m}\|\mathbf{A}^H(\theta_m)\mathbf{x}\|^2}{\max_{\vartheta_s}\|\mathbf{A}^H(\vartheta_s)\mathbf{x}\|^2} \\ \text{s.t. }& \theta_m \in \Theta, \vartheta_s \in \Omega, \\ & |x(\bar{n})| = \xi,\ \bar{n} = 1, \cdots, LN, \end{aligned} \tag{6}$$

where ξ is a given parameter (e.g., $\xi = 1$). Obviously, (6) implies that the MML acts as the power reference point and the normalized minimum PSL property is achieved via maximizing the ratio of the MML to the PSL. However, (6) is a complicated and coupled QFP problem since both of the numerator and denominator are the functions of $\mathbf{x}$. Besides, (6) is nonconvex due to the CM constraints $|x(\bar{n})| = \xi$, for $\bar{n} = 1, \cdots, LN$. In Section III.A, we derive an equivalent formulation of (6) and develop a new method to solve this challenging nonconvex optimization problem.

2) With Ripple Constraints Design (WRC-Design): In the second problem formulation, we consider designing MPSTB with the mainlobe ripple constraints. Specifically, the transmit power in the mainlobe region should satisfy $d - \varepsilon_r \le \|\mathbf{A}^H(\theta_m)\mathbf{x}\|^2 \le d + \varepsilon_r$ for all $\theta_m \in \Theta$, where ε_r is the ripple term, and d is the desired mainlobe level. However, there exists an uncertain scaling factor between the pattern mask and actual transmit beampattern due to CM constraints on waveform (see Eq. (19) of [2] and Eq. (16) of [12] for details). We rewrite (5) as $x(\bar{n}) = \xi e^{j\angle x(\bar{n})}$, for $\bar{n} = 1, \cdots, LN$. With (4), we have

$$P(\theta) = \xi^2\left(e^{j\angle \mathbf{x}}\right)^H \mathbf{A}(\theta)\mathbf{A}^H(\theta)e^{j\angle \mathbf{x}}. \tag{7}$$

Obviously, ξ is related to the scaling factor, and can be used to avoid the scaling problem. Thus, the design problem, referred to as WRC-design, is formulated as

$$\begin{aligned} \min_{\xi,\mathbf{x}}\ & \max_{\vartheta_s\in\Omega}\|\mathbf{A}^H(\vartheta_s)\mathbf{x}\|^2 \\ \text{s.t. }& d - \varepsilon_r \le \|\mathbf{A}^H(\theta_m)\mathbf{x}\|^2 \le d + \varepsilon_r, \theta_m \in \Theta, \\ & |x(\bar{n})| = \xi\ ,\ \bar{n} = 1, \cdots, LN. \end{aligned} \tag{8}$$

Note that (8) is also nonconvex, since the double-sided quadratic and CM constraints form a nonconvex set. In Section III.B, we develop an efficient optimization method to tackle this nonconvex problem.

Remark: In (8), the waveform modulus ξ is set as an unknown variable to make the design problem feasible. Thus in radar engineering applications, a postprocessing procedure is utilized to adjust the obtained modulus ξ to an expected (or given) magnitude level (e.g., $\tilde{\xi}$) in this problem formulation. Even if the designed waveform vector $\mathbf{x}$ becomes $\frac{\tilde{\xi}}{\xi}\mathbf{x}$ and the referenced mainlobe level d becomes $\frac{\tilde{\xi}^2}{\xi^2}d$ after the postprocessing procedure, the ratio of the PSL to the referenced mainlobe level still remains unchanged, i.e.,

$$\frac{\max_{\vartheta_s\in\Omega}\|\mathbf{A}^H(\vartheta_s)\mathbf{x}\|^2}{d} = \frac{\max_{\vartheta_s\in\Omega}\|\mathbf{A}^H(\vartheta_s)\frac{\tilde{\xi}}{\xi}\mathbf{x}\|^2}{\frac{\tilde{\xi}^2}{\xi^2}d}.$$

In addition, both the upper bound $d+\varepsilon_r$ and the lower bound $d-\varepsilon_r$ of the mainlobe levels are increased to $\frac{\tilde{\xi}^2}{\xi^2}$ times, while their ratio still remains unchanged.

III. Algorithms for MIMO Radar Transmit Beampattern Design Metrics

In this section, two efficient optimization algorithms, named WBM-design algorithm and WRC-design algorithm, are derived to solve design metrics in (6) and (8), respectively. In the rest of the paper, the symbols $\mathbf{A}(\vartheta_s)$ and $\mathbf{A}(\theta_m)$ are simplified as $\mathbf{\Lambda}_s$ and $\mathbf{A}_m$, respectively.

A. WBM-Design Algorithm

To decouple the numerator and denominator in (6), we first introduce two boundary-type auxiliary variables, named PSL η and MML ε and transform (6) as the following equivalent problem:

$$\begin{aligned}\max_{\mathbf{x},\varepsilon,\eta}\ & \frac{\varepsilon}{\eta}\\ \text{s.t. } & |x(\bar{n})|=1,\ \ \bar{n}=1,\cdots,LN,\\ & \|\mathbf{\Lambda}_s^H\mathbf{x}\|^2\le\eta,\ \ s=1,\cdots,S,\\ & \|\mathbf{A}_m^H\mathbf{x}\|^2\ge\varepsilon,\ \ m=1,\cdots,M.\end{aligned}\tag{9}$$

Then, to separate ε and η in the fractional operation, we replace the objective function in (9) with

$$\min_{\mathbf{x},\varepsilon,\eta}\ -\log\left(\frac{\varepsilon}{\eta}\right).\tag{10}$$

Obviously, after the equivalent transformation, the complex fraction-like objective function is simplified into $\log(\eta)-\log(\varepsilon)$. However, the vector variable $\mathbf{x}$ is still subject to both the complicated CM constraints $|x(\bar{n})|=1$ and complex quadratic inequality constraints $\|\mathbf{\Lambda}_s^H\mathbf{x}\|^2\le\eta$ and $\|\mathbf{A}_m^H\mathbf{x}\|^2\ge\varepsilon$. To tackle two kinds of constraints separately and simplify the optimization problem, we introduce several linear equality constraints $\mathbf{y}_s=\mathbf{\Lambda}_s^H\mathbf{x}$ and $\mathbf{z}_m=\mathbf{A}_m^H\mathbf{x}$ with auxiliary variables $\mathbf{y}_s$ and $\mathbf{z}_m$, for $s=1,\cdots,S$ and $m=1,\cdots,M$, and rewrite (9) as

$$\begin{aligned}\min_{\mathbf{x},\varepsilon,\eta,\{\mathbf{y}_s\},\{\mathbf{z}_m\}}\ & -\log\left(\frac{\varepsilon}{\eta}\right)\\ \text{s.t. } & |x(\bar{n})|=1,\ \ \bar{n}=1,\cdots,LN,\\ & \mathbf{y}_s=\mathbf{\Lambda}_s^H\mathbf{x},\|\mathbf{y}_s\|^2\le\eta,s=1,\cdots,S,\\ & \mathbf{z}_m=\mathbf{A}_m^H\mathbf{x},\|\mathbf{z}_m\|^2\ge\varepsilon,m=1,\cdots,M.\end{aligned}\tag{11}$$

Clearly, (11) indicates that the variable $\mathbf{x}$ is under the linear equality and CM constraints, whereas the auxiliary variables $\mathbf{y}_s$ and $\mathbf{z}_m$ are subject to the quadratic constraints $\|\mathbf{y}_s\|^2\le\eta$ and $\|\mathbf{z}_m\|^2\ge\varepsilon$, for $s=1,\cdots,S$ and $m=1,\cdots,M$, respectively.

Note that the constraints $\|\mathbf{y}_s\|^2\le\eta$ and $\|\mathbf{z}_m\|^2\ge\varepsilon$ will play their roles in determining $\mathbf{y}_s$ and $\mathbf{z}_m$, for $s=1,\cdots,S$ and $m=1,\cdots,M$, and the CM constraints $|x(\bar{n})|=1$, for $\bar{n}=1,\cdots,LN$, functions in the determination of $\mathbf{x}$. Therefore, the augmented Lagrangian (using the scaled dual variables) [29] of (11) is defined as:

$$\begin{aligned}L_\rho(\mathbf{x},\mathbf{y}_s,\eta,\mathbf{z}_m,\varepsilon,\boldsymbol{\lambda}_s,\boldsymbol{\nu}_m)&=\log\left(\frac{\eta}{\varepsilon}\right)\\ &+\frac{\rho}{2}\sum_{s=1}^{S}(\|\mathbf{y}_s-\mathbf{\Lambda}_s^H\mathbf{x}+\boldsymbol{\lambda}_s\|^2-\|\boldsymbol{\lambda}_s\|^2)\\ &+\frac{\rho}{2}\sum_{m=1}^{M}(\|\mathbf{z}_m-\mathbf{A}_m^H\mathbf{x}+\boldsymbol{\nu}_m\|^2-\|\boldsymbol{\nu}_m\|^2),\end{aligned}\tag{12}$$

where $\rho>0$ is the step size, and $\boldsymbol{\lambda}_s\in\mathbb{C}^{N\times1},\boldsymbol{\nu}_m\in\mathbb{C}^{N\times1}$, for $s=1,\cdots,S,m=1,\cdots,M$, are the scaled dual variables [29]. Then, the alternating direction method of multipliers is applied into (11) to determine $\{\mathbf{x},\mathbf{y}_s,\eta,\mathbf{z}_m,\varepsilon,\boldsymbol{\lambda}_s,\boldsymbol{\nu}_m\}$ via the following iterative steps:

$$\mathbf{x}^{t+1}:=\arg\min_{\mathbf{x}}L_\rho(\mathbf{x},\mathbf{y}_s^t,\eta^t,\mathbf{z}_m^t,\varepsilon^t,\boldsymbol{\lambda}_s^t,\boldsymbol{\nu}_m^t)\quad\text{s.t. }|x(\bar{n})|=1,\ \bar{n}=1,\cdots,LN;\tag{13a}$$

$$\{\mathbf{y}_s^{t+1},\eta^{t+1}\}:=\arg\min_{\{\mathbf{y}_s\},\eta}L_\rho(\mathbf{x}^{t+1},\mathbf{y}_s,\eta,\mathbf{z}_m^t,\varepsilon^t,\boldsymbol{\lambda}_s^t,\boldsymbol{\nu}_m^t)\quad\text{s.t. }\|\mathbf{y}_s\|^2\le\eta,s=1,\cdots,S;\tag{13b}$$

$$\{\mathbf{z}_m^{t+1},\varepsilon^{t+1}\}:=\arg\min_{\{\mathbf{z}_m\},\varepsilon}L_\rho(\mathbf{x}^{t+1},\mathbf{y}_s^t,\eta^t,\mathbf{z}_m,\varepsilon,\boldsymbol{\lambda}_s^t,\boldsymbol{\nu}_m^t)\quad\text{s.t. }\|\mathbf{z}_m\|^2\ge\varepsilon,m=1,\cdots,M;\tag{13c}$$

$$\boldsymbol{\lambda}_s^{t+1}:=\boldsymbol{\lambda}_s^t+\mathbf{y}_s^{t+1}-\mathbf{\Lambda}_s^H\mathbf{x}^{t+1},s=1,\cdots,S;\tag{13d}$$

$$\boldsymbol{\nu}_m^{t+1}:=\boldsymbol{\nu}_m^t+\mathbf{z}_m^{t+1}-\mathbf{A}_m^H\mathbf{x}^{t+1},m=1,\cdots,M;\tag{13e}$$

where t is the number of iterations.

Obviously, the complicated optimization problem in (6) is split into several subproblems (13a)–(13e), where the first $\mathbf{x}$-update subproblem in (13a) is subject to only the CM constraints; whereas both the $\{\mathbf{y}_s,\eta\}$-update subproblem in (13b) and $\{\mathbf{z}_m,\varepsilon\}$-update subproblem in (13c) are only under quadratic inequality constraints. The last two steps in (13d) and (13e) are the commonly update rules of scaled dual variables $\{\boldsymbol{\lambda}_s\}$ and $\{\boldsymbol{\nu}_m\}$ (see [29] for details). Additionally, the $\mathbf{y}_s$- and $\mathbf{z}_m$-updates can be carried out independently in parallel for each s and m, whereas $\{\boldsymbol{\lambda}_s\}$ and $\{\boldsymbol{\nu}_m\}$ can be updated in parallel via the computations in (13d) and (13e).

The solutions to the subproblems in (13a)–(13c) are derived in detail as follows.

1) Solution to (13a): With the given $\{\mathbf{y}_s^t,\eta^t,\mathbf{z}_m^t,\varepsilon^t,\boldsymbol{\lambda}_s^t,\boldsymbol{\nu}_m^t\}$, and by ignoring irrelevant items in (13a), the optimization problem in (13a) reduces to

$$\begin{aligned}\min_{\mathbf{x}}\ & \sum_{s=1}^{S}\|\mathbf{u}_s^t-\mathbf{\Lambda}_s^H\mathbf{x}\|^2+\sum_{m=1}^{M}\|\mathbf{h}_m^t-\mathbf{A}_m^H\mathbf{x}\|^2\\ \text{s.t. } & |x(\bar{n})|=1,\ \ \bar{n}=1,\cdots,LN,\end{aligned}\tag{14}$$

where $\mathbf{u}_s^t=\mathbf{y}_s^t+\boldsymbol{\lambda}_s^t$, for $s=1,\cdots,S$, and $\mathbf{u}_m^t=\mathbf{z}_m^t+\boldsymbol{\nu}_m^t$, for $m=1,\cdots,M$.

To simplify (14), we define $\mathbf{A}_{M+s} = \mathbf{\Lambda}_s$ and $\mathbf{h}_{M+s}^t = \mathbf{u}_s^t$, for $s = 1, \cdots, S$, and rewrite (14) in a compact form as

$$\min_{\mathbf{x}} \sum_{p=1}^{P} \|\mathbf{u}_p^t - \mathbf{A}_p^H \mathbf{x}\|^2$$
$$\text{s.t. } |x(\bar{n})| = 1, \ \ \bar{n} = 1, ..., LN, \tag{15}$$

where $P = M + S$.

The CM constraints ($|x(\bar{n})| = 1, \bar{n} = 1, ..., LN$) make (15) become a general NP-hard unimodular quadratic program (UQP) problem [36], [37]. To tackle this challenging nonconvex problem, we simplify the CM constraints via introducing auxiliary phase variables $\boldsymbol{\phi} = [\phi(1), \cdots, \phi(LN)]^T$ such that (15) is converted into the following optimization problem without modulus operation:

$$\min_{\mathbf{x}, \boldsymbol{\phi}} \sum_{p=1}^{P} \|\mathbf{h}_p^t - \mathbf{A}_p^H \mathbf{x}\|^2 \ \text{ s.t. } \mathbf{x} = e^{j\boldsymbol{\phi}}, \tag{16}$$

the scaled form augmented Lagrangian of which is given by:

$$L_\alpha(\boldsymbol{\phi}, \mathbf{x}, \boldsymbol{\gamma}) = \sum_{p=1}^{P} \|\mathbf{h}_p^t - \mathbf{A}_p^H \mathbf{x}\|^2 + \frac{\alpha}{2}(\|\mathbf{x} - e^{j\boldsymbol{\phi}} + \boldsymbol{\gamma}\|^2 - \|\boldsymbol{\gamma}\|^2), \tag{17}$$

where $\alpha > 0$ and $\boldsymbol{\gamma} \in \mathbb{C}^{LN \times 1}$ are the step size and scaled dual variable, respectively.

Then, the following iterative steps derived from the alternating direction method of multipliers in (17) are applied to solve (16):

$$\boldsymbol{\phi}^{i+1} := \arg\min_{\boldsymbol{\phi}} L_\alpha(\boldsymbol{\phi}, \mathbf{x}^i, \boldsymbol{\gamma}^i), \tag{18a}$$

$$\mathbf{x}^{i+1} := \arg\min_{\mathbf{x}} L_\alpha(\boldsymbol{\phi}^{i+1}, \mathbf{x}, \boldsymbol{\gamma}^i), \tag{18b}$$

$$\boldsymbol{\gamma}^{i+1} := \boldsymbol{\gamma}^i + \mathbf{x}^{i+1} - e^{j\boldsymbol{\phi}^{i+1}}, \tag{18c}$$

where i is the number of iterations.

With the definition $\mathbf{b}^i = \mathbf{x}^i + \boldsymbol{\gamma}^i$, the $\boldsymbol{\phi}$-update problem in (18a) reduces to

$$\min_{\boldsymbol{\phi}} \|\mathbf{b}^i - e^{j\boldsymbol{\phi}}\|^2, \tag{19}$$

the solution to which is given by:

$$\boldsymbol{\phi}^{i+1} = \angle \mathbf{b}^i. \tag{20}$$

Similarly, with the definition $\hat{\mathbf{x}}^i = e^{j\boldsymbol{\phi}^{i+1}} - \boldsymbol{\gamma}^i$ and ignoring the constant terms in (18b) yields

$$\min_{\mathbf{x}} \sum_{p=1}^{P} \|\mathbf{h}_p^t - \mathbf{A}_p^H \mathbf{x}\|^2 + \frac{\alpha}{2}\|\mathbf{x} - \hat{\mathbf{x}}^i\|^2. \tag{21}$$

Lemma 1: The solution to (21) is given by

$$\mathbf{x}^{i+1} = \left(\mathbf{I}_N \otimes \mathbf{Z}_\alpha^{-1}\right)\mathbf{q}, \tag{22}$$

where $\mathbf{Z}_\alpha = \sum_{p=1}^{P} \mathbf{a}(\theta_p)\mathbf{a}^H(\theta_p) + \frac{\alpha}{2}\mathbf{I}_L \in \mathbb{C}^{L \times L}$ and $\mathbf{q} = \sum_{p=1}^{P} \mathbf{A}_p \mathbf{h}_p^t + \hat{\mathbf{x}}^i$.

Proof: See Appendix A.

Algorithm 1: Solution to (13a).

Input: $\{\mathbf{u}_p^t\}$, step size α, iteration stop tolerance ζ, and the maximum iteration number I.

Initialization: $\boldsymbol{\phi}^0, \boldsymbol{\gamma}^0, i = 0$.

1: **while** $\|\mathbf{x}^i - e^{j\boldsymbol{\phi}^i}\| > \zeta$ and $i < I$ **do**
2: Obtain $\boldsymbol{\phi}^{i+1}$ using (20);
3: Obtain $\mathbf{x}^{i+1}$ using (22);
4: Update $\boldsymbol{\gamma}^{i+1}$ using (18c);
5: $i = i + 1$.
6: **end while**

Output: MIMO radar waveform vector $\mathbf{x}^{i+1}$.

Thus, we summarize the algorithm shown in (14)–(22) as Algorithm 1.

2) Solution to (13b): Ignoring the constant terms in (13b), we have

$$\min_{\{\mathbf{y}_s\}, \eta} \ \log(\eta) + \frac{\rho}{2}\sum_{s=1}^{S} \|\mathbf{y}_s - \hat{\mathbf{y}}_s^t\|^2$$
$$\text{s.t. } \|\mathbf{y}_s\|^2 \le \eta, s = 1, \cdots, S, \tag{23}$$

where $\hat{\mathbf{y}}_s^t = \mathbf{\Lambda}_s^H \mathbf{x}^{t+1} - \boldsymbol{\lambda}_s^t$, for $s = 1, \cdots, S$.

We can see from (23) that η is coupled with $\{\mathbf{y}_s\}$ in the constraints $\|\mathbf{y}_s\|^2 \le \eta$. However, once η^{t+1} is provided, the optimal $\mathbf{y}_s^{t+1}$ is obtained by solving the following subproblem:

$$\min_{\mathbf{y}_s} \ \|\mathbf{y}_s - \hat{\mathbf{y}}_s^t\|^2 \ \ \text{s.t. } \|\mathbf{y}_s\|^2 \le \eta^{t+1}, \tag{24}$$

for $s = 1, \cdots, S$.

Lemma 2: the solution to (24) is given by

$$\mathbf{y}_s^{t+1} = \begin{cases} \sqrt{\eta^{t+1}}\frac{\hat{\mathbf{y}}_s^t}{\|\hat{\mathbf{y}}_s^t\|}, & \text{if } \|\hat{\mathbf{y}}_s^t\| > \sqrt{\eta^{t+1}}, \\ \hat{\mathbf{y}}_s^t, & \text{otherwise.} \end{cases} \tag{25}$$

Proof: See Appendix B.

Similarly, if $\vartheta_{\bar{s}}$ is set to be null or notch with the depth ι (see Exp. 4 for details), the optimal $\mathbf{y}_{\bar{s}}^{t+1}$ is given by

$$\mathbf{y}_{\bar{s}}^{t+1} = \begin{cases} \sqrt{\iota}\frac{\hat{\mathbf{y}}_{\bar{s}}^t}{\|\hat{\mathbf{y}}_{\bar{s}}^t\|}, & \text{if } \|\hat{\mathbf{y}}_{\bar{s}}^t\| > \sqrt{\iota}, \\ \hat{\mathbf{y}}_{\bar{s}}^t, & \text{otherwise.} \end{cases} \tag{26}$$

Then, we consider utilizing the result in (25) to solve (23). Substituting (25) into the objective function in (23) yields an optimization problem of a single variable η:

$$\min_{\eta} \ f(\eta), \tag{27}$$

where $f(\eta) = \log(\eta) + \frac{\rho}{2}\sum_{s=1}^{S} w_s(\sqrt{\eta} - \|\hat{\mathbf{y}}_s^t\|)^2$. Additionally, $w_s = 0$, if $\|\hat{\mathbf{y}}_s^t\| \le \sqrt{\eta}$; otherwise $w_s = 1$.

With $[\hat{\eta}_0, \hat{\eta}_1, \cdots, \hat{\eta}_K]$ as the ascending order sequence of $[\|\hat{\mathbf{y}}_1^t\|, \|\hat{\mathbf{y}}_2^t\|, \cdots, \|\hat{\mathbf{y}}_S^t\|]$, where $K \le S$ (removing repetitions), (27) can be represented as a piecewise function:

$$f(\eta) = \{f_k(\eta) | \hat{\eta}_{k-1} \le \sqrt{\eta} \le \hat{\eta}_k, k = 1, \cdots, K\}, \tag{28}$$

where $f_k(\eta) = \log(\eta) + \frac{\rho}{2}\sum_{n=k}^{K}(\sqrt{\eta} - \hat{\eta}_n)^2$ is defined in the region $[\hat{\eta}_{k-1}, \hat{\eta}_k]$. Note that the first term $\log(\eta)$ is concave and the second term $\frac{\rho}{2}\sum_{n=k}^{K}(\sqrt{\eta} - \hat{\eta}_n)^2$ is convex, Therefore, the function $f_k(\eta)$ is nonconvex [41]. In order to tackle this

nonconvex problem, we introduce an auxiliary variable $\mu = \sqrt{\eta}$, where $\mu > 0$, and transform the kth piecewise function $f_k(\eta)$ into that of μ, i.e.,

$$f_k(\mu) = 2\log(\mu) + \frac{\rho}{2}\sum_{n=k}^{K}\mu^2 - \rho\sum_{n=k}^{K}\hat{\eta}_n\mu + \frac{\rho}{2}\sum_{n=k}^{K}\hat{\eta}_n^2, \quad (29)$$

the first and third derivatives of which with respect to μ are given by:

$$f_k^{'}(\mu) = 2\mu^{-1} + \rho\sum_{n=k}^{K}\mu - \rho\sum_{n=k}^{K}\hat{\eta}_n,$$
$$f_k^{'''}(\mu) = 4\mu^{-3} > 0, \quad (30)$$

respectively.

Since $f_k^{'''}(\mu) > 0$, $f_k^{'}(\mu)$ is convex for the subregion $\mu \in [\hat{\eta}_{k-1}, \hat{\eta}_k]$. In order to get the minimal value point of $f_k(\mu)$, we set $f_k^{'}(\mu)$ as zero, i.e.,

$$a\mu^2 + b\mu + c = 0, \quad (31)$$

where $a = \sum_{n=k}^{K}\rho$, $b = -\rho\sum_{n=k}^{K}\hat{\eta}_n$, and $c = 2$. The two real roots υ_1, υ_2 of (31) are given, respectively, by:

$$\upsilon_1 = \frac{-b - \sqrt{b^2 - 4ac}}{2a},\ \upsilon_2 = \frac{-b + \sqrt{b^2 - 4ac}}{2a}. \quad (32)$$

Thus, the minimal value of the kth subfunction $f_k(\mu)$ in the region $\mu \in [\hat{\eta}_{k-1}, \hat{\eta}_k]$ can be determined from different cases:

Case 1: if $b^2 - 4ac \le 0$ (there do not exist real roots) or $b^2 - 4ac \ge 0$ ($\upsilon_1 \le \upsilon_2 \le \hat{\eta}_{k-1} \le \hat{\eta}_k$ or $\hat{\eta}_{k-1} \le \hat{\eta}_k \le \upsilon_1 \le \upsilon_2$), the function $f_k(\mu)$ is monotonically increasing on the interval $[\hat{\eta}_{k-1}, \hat{\eta}_k]$, and thus $f_k(\mu)$ achieves its minimum at $\mu_k = \hat{\eta}_{k-1}$.

Case 2: if $b^2 - 4ac > 0$ and $\upsilon_1 \le \hat{\eta}_{k-1} \le \hat{\eta}_k \le \upsilon_2$, the function $f_k(\mu)$ is monotonically decreasing on the interval $[\hat{\eta}_{k-1}, \hat{\eta}_k]$, and thus $f_k(\mu)$ achieves its minimum at $\mu_k = \hat{\eta}_k$.

Case 3: if $b^2 - 4ac > 0$ and $\upsilon_1 \le \hat{\eta}_{k-1} \le \upsilon_2 \le \hat{\eta}_k$, the function $f_k(\mu)$ is monotonically decreasing in $[\hat{\eta}_{k-1}, \upsilon_2]$ and increasing in $[\upsilon_2, \hat{\eta}_k]$. Therefore, $f_k(\mu)$ achieves its minimum at $\mu_k = \upsilon_2$.

Case 4: if $b^2 - 4ac > 0$ and $\hat{\eta}_{k-1} \le \upsilon_1 \le \upsilon_2 \le \hat{\eta}_k$, the function $f_k(\mu)$ is monotonically increasing in $[\hat{\eta}_{k-1}, \upsilon_1] \cup [\upsilon_2, \hat{\eta}_k]$ and decreasing in $[\upsilon_1, \upsilon_2]$. Therefore, $f_k(\mu)$ achieves its minimum at $\mu_k = \arg\min_{\mu}\{f_k(\hat{\eta}_{k-1}), f_k(\upsilon_2)\}$.

Case 5: otherwise (i.e., $b^2 - 4ac > 0$ and $\hat{\eta}_{k-1} \le \upsilon_1 \le \hat{\eta}_k \le \upsilon_2$), the function $f_k(\mu)$ is monotonically increasing in $[\hat{\eta}_{k-1}, \upsilon_1]$ and decreasing in $[\upsilon_1, \hat{\eta}_k]$. Therefore, $f_k(\mu)$ achieves its minimum at $\mu_k = \arg\min_{\mu}\{f_k(\hat{\eta}_{k-1}), f_k(\hat{\eta}_k)\}$.

Inserting the optimal μ_k from the aforementioned cases into (28), the potential local minimal function value of (27) is achieved, denoted by $f_k(\mu_k)$. By selecting the globally minimum value from all the K locally minimal values of K piecewise functions, we obtain the optimal η^{t+1} as

$$\eta^{t+1} = \{\arg\min_{\mu_k}\{f_1(\mu_1), f_2(\mu_2), \cdots, f_K(\mu_K)\}\}^2. \quad (33)$$

Then, inserting η^{t+1} into (25) yields the optimal $\{\mathbf{y}_s^{t+1}\}$.

3) Solution to (13c): Ignoring the constant terms in (13c), we have

$$\min_{\{\mathbf{z}_m\},\varepsilon} \ -\log(\varepsilon) + \frac{\rho}{2}\sum_{m=1}^{M}\|\mathbf{z}_m - \hat{\mathbf{z}}_m^t\|^2$$
$$\text{s.t. } \|\mathbf{z}_m\|^2 \ge \varepsilon, m = 1, \cdots, M, \quad (34)$$

where $\hat{\mathbf{z}}_m^t = \mathbf{A}_m^H\mathbf{x}^{t+1} - \boldsymbol{\nu}_m^t$ for $m = 1, \cdots, M$, and ε is coupled with $\{\mathbf{z}_m\}$. However, once ε^{t+1} is provided, the optimal $\mathbf{z}_m^{t+1}$ is given by the solution of the following problem:

$$\min_{\mathbf{z}_m} \ \|\mathbf{z}_m - \hat{\mathbf{z}}_m^t\|^2 \quad \text{s.t. } \|\mathbf{z}_m\|^2 \ge \varepsilon^{t+1}, \quad (35)$$

for $m = 1, \cdots, M$. According to Lemma 2, the solution to (35) is given by

$$\mathbf{z}_m^{t+1} = \begin{cases} \hat{\mathbf{z}}_m^t, & \text{if } \|\hat{\mathbf{z}}_m^t\| > \sqrt{\varepsilon^{t+1}}, \\ \sqrt{\varepsilon^{t+1}}\frac{\hat{\mathbf{z}}_m^t}{\|\hat{\mathbf{z}}_m^t\|}, & \text{otherwise.} \end{cases} \quad (36)$$

Substituting (36) into (34) yields another optimization problem of a single variable ε:

$$\min_{\varepsilon} \ g(\varepsilon), \quad (37)$$

where $g(\varepsilon) = -\log(\varepsilon) + \frac{\rho}{2}\sum_{m=1}^{M}\hat{w}_m(\sqrt{\varepsilon} - \|\hat{\mathbf{z}}_m^t\|)^2$. Additionally, $\hat{w}_m = 0$ if $\|\hat{\mathbf{z}}_m^t\| \ge \sqrt{\varepsilon}$; otherwise $\hat{w}_m = 1$.

With $[\epsilon_0, \epsilon_1, \cdots, \epsilon_K]$ as the ascending order sequence of $[\|\hat{\mathbf{z}}_1^t\|, \|\hat{\mathbf{z}}_2^t\|, \cdots, \|\hat{\mathbf{z}}_M^t\|]$, where $K \le M$ (removing repetitions), (37) can be expressed in a piecewise function as:

$$g(\varepsilon) = \{g_k(\varepsilon) | \epsilon_{k-1} \le \sqrt{\varepsilon} \le \epsilon_k, k = 1, \cdots, K\}, \quad (38)$$

where $g_k(\varepsilon) = -\log(\varepsilon) + \frac{\rho}{2}\sum_{n=1}^{k}(\sqrt{\varepsilon} - \epsilon_n)^2$ is defined in the region $[\epsilon_{k-1}, \epsilon_k]$. Since both $-\log(\varepsilon)$ and $\frac{\rho}{2}\sum_{n=1}^{k}(\sqrt{\varepsilon} - \epsilon_n)^2$ with respect to ε are convex, (38) is also convex [41]. To remove the square root operation and simplify the following analysis, we introduce a new variable $\varsigma = \sqrt{\varepsilon}$, where $\varsigma > 0$, and represent the kth piecewise function $g_k(\varepsilon)$ into that of ς:

$$g_k(\varsigma) = -2\log(\varsigma) + \frac{\rho}{2}\sum_{n=1}^{k}\varsigma^2 - \rho\sum_{n=1}^{k}\epsilon_n\varsigma + \frac{\rho}{2}\sum_{n=1}^{k}\epsilon_n^2. \quad (39)$$

Setting the first derivative of (39) with respect to ς as zero, i.e, $g_k^{'}(\varsigma) = 0$, we have:

$$\bar{a}_k\varsigma^2 + \bar{b}_k\varsigma + \bar{c}_k = 0, \quad (40)$$

where $\varsigma > 0$, $\bar{a}_k = \rho\sum_{n=1}^{k}1 > 0$, $\bar{b}_k = -\rho\sum_{n=1}^{k}\epsilon_n < 0$, and $\bar{c}_k = -2$. Obviously, $-4\bar{a}_k\bar{c}_k > 0$, and the non-negative root of (40) is given by $\varsigma_1 = \frac{-\bar{b}_k + \sqrt{\bar{b}_k^2 - 4\bar{a}_k\bar{c}_k}}{2\bar{a}_k}$.

According to the convexity of $g(\varsigma)$ and its first derivative, it is easily found that $g_k^{'}(\varsigma)$ is a monotonous function at the subregion $\varsigma \in [\epsilon_{k-1}, \epsilon_k]$. Thus, the minimum value of the kth piecewise function in the region $\varsigma \in [\epsilon_{k-1}, \epsilon_k]$ is determined from the following cases:

Case 1: if $g_k^{'}(\epsilon_{k-1}) > 0$, the optimal value of $g_k(\varsigma)$ is achieved at $\omega_k = \epsilon_{k-1}$.

Case 2: if $g_k^{'}(\epsilon_k) < 0$, the optimal value of $g_k(\varsigma)$ is achieved at $\omega_k = \epsilon_k$.

Algorithm 2: WBM-design Algorithm.

Input: Step size ρ, and the maximum iteration number T_0, iteration stop tolerance $\tilde{\iota}$, mainlobe region Θ, and sidelobe region Ω.

Initialization: $\{\mathbf{y}_s^0\}, \{\mathbf{z}_m^0\}, \{\boldsymbol{\lambda}_s^0\}, \{\boldsymbol{\nu}_m^0\}, t = 0$.

1: **while** $|\varepsilon^{t+1} - \varepsilon^t| > \tilde{\iota}$ and $t \le T_0$ **do**
2: Obtain $\mathbf{x}^{t+1}$ using **Algorithm 1**;
3: Determine $\eta^{t+1}, \{\mathbf{y}_s^{t+1}\}$ using (33), (25) or (26), respectively;
Determine $\varepsilon^{t+1}, \{\mathbf{z}_m^{t+1}\}$ using (41) and (36), respectively;
4: Update $\{\boldsymbol{\lambda}_s^{t+1}\}, \{\boldsymbol{\nu}_m^{t+1}\}$ using (13d) and (13e), respectively;
5: $t = t + 1$.
6: **end while**

Output: MIMO radar waveform vector $\mathbf{x}$.

Case 3: if $g_k^{'}(\epsilon_{k-1}) < 0$ and $g_k^{'}(\epsilon_k) > 0$, the optimal value of $g_k(\varsigma)$ is achieved at $\omega_k = \varsigma_1$.

Inserting ω_k into (38), we obtain the potential minimal value of the kth subfunction, denoted as $g_k(\omega_k)$. By selecting the global minimal value from all the K locally minimal piecewise function values, we obtain the optimal ε^{t+1} as

$$\varepsilon^{t+1} = \{\arg\min_{\omega_k}\{g_1(\omega_1), g_2(\omega_2), \cdots g_K(\omega_K)\}\}^2. \quad (41)$$

Then, inserting ε^{t+1} into (36) yields the optimal $\{\mathbf{z}_m^{t+1}\}$.

We summarize the proposed WBM-design algorithm in Algorithm 2.

B. WRC-Design Algorithm

First we introduce a boundary-type auxiliary variable η to simplify the objective function in (8), and rewrite (8) as:

$$\begin{aligned}\min_{\xi,\mathbf{x},\eta}\ & \eta \\ \text{s.t. } & |x(\bar{n})| = \xi\ ,\ \ \bar{n} = 1, \cdots, LN; \\ & \|\boldsymbol{\Lambda}_s^H \mathbf{x}\|^2 \le \eta, s = 1, \cdots, S; \\ & d - \varepsilon_r \le \|\mathbf{A}_m^H \mathbf{x}\|^2 \le d + \varepsilon_r, m = 1, \cdots, M. \end{aligned} \quad (42)$$

Clearly, $\mathbf{x}$ is subject to the quadratic inequality constraints $\|\boldsymbol{\Lambda}_s^H \mathbf{x}\|^2 \le \eta$, double-sided constraints $d - \varepsilon_r \le \|\mathbf{A}_m^H \mathbf{x}\|^2 \le d + \varepsilon_r$, and CM constraints $|x(\bar{n})| = \xi$. To tackle the aforementioned complicated constraints separately, we introduce several linear equality constraints $\mathbf{g}_s = \boldsymbol{\Lambda}_s^H \mathbf{x}$ and $\mathbf{w}_m = \mathbf{A}_m^H \mathbf{x}$ with auxiliary variables $\mathbf{g}_s$ and $\mathbf{w}_m$, for $s = 1, \cdots, S$, and $m = 1, \cdots, M$. Thus, we transform (42) into the following equivalent optimization problem:

$$\begin{aligned}\min_{\xi,\mathbf{x},\{\mathbf{g}_s\},\eta,\{\mathbf{w}_m\}}\ & \eta \\ \text{s.t. } & \mathbf{g}_s = \boldsymbol{\Lambda}_s^H \mathbf{x}, \|\mathbf{g}_s\|^2 \le \eta, s = 1, \cdots, S; \\ & \mathbf{w}_m = \mathbf{A}_m^H \mathbf{x}, d - \varepsilon_r \le \|\mathbf{w}_m\|^2 \le d + \varepsilon_r, \\ & m = 1, \cdots, M; |x(\bar{n})| = \xi, \bar{n} = 1, \cdots, LN. \end{aligned} \quad (43)$$

In the same way as the WBM-design algorithm, the augmented Lagrangian (scaled form) [29] of (43) is defined as:

$$\begin{aligned} L_\beta(\xi, \mathbf{x}, \mathbf{g}_s, \eta, \mathbf{w}_m, \boldsymbol{\lambda}_s, \boldsymbol{\nu}_m) &= \eta \\ &+ \frac{\beta}{2}\sum_{s=1}^{S}(\|\mathbf{g}_s - \boldsymbol{\Lambda}_s^H \mathbf{x} + \boldsymbol{\lambda}_s\|^2 - \|\boldsymbol{\lambda}_s\|^2) \\ &+ \frac{\beta}{2}\sum_{m=1}^{M}(\|\mathbf{w}_m - \mathbf{A}_m^H \mathbf{x} + \boldsymbol{\nu}_m\|^2 - \|\boldsymbol{\nu}_m\|^2), \end{aligned} \quad (44)$$

where $\boldsymbol{\lambda}_s \in \mathbb{C}^{N\times 1}$, for $s = 1, \cdots, S$, and $\boldsymbol{\nu}_m \in \mathbb{C}^{N\times 1}$, for $m = 1, \cdots, M$, are the scaled dual variables, and $\beta > 0$ is the step size. Then, we determine $\{\xi, \mathbf{x}, \mathbf{g}_s, \eta, \mathbf{w}_m, \boldsymbol{\lambda}_s, \boldsymbol{\nu}_m\}$ from (44) via the following iterative steps:

$$\{\mathbf{x}^{t+1}, \xi^{t+1}\} := \arg\min_{\mathbf{x},\xi} L_\beta(\xi, \mathbf{x}, \mathbf{g}_s^t, \eta^t, \mathbf{w}_m^t, \boldsymbol{\lambda}_s^t, \boldsymbol{\nu}_m^t)$$
$$\text{s.t. } |x(\bar{n})| = \xi,\ \bar{n} = 1, \cdots, LN; \quad (45a)$$

$$\{\mathbf{g}_s^{t+1}, \eta^{t+1}\} := \arg\min_{\{\mathbf{g}_s\},\eta} L_\beta(\xi^{t+1}, \mathbf{x}^{t+1}, \mathbf{g}_s, \eta, \mathbf{w}_m^t, \boldsymbol{\lambda}_s^t, \boldsymbol{\nu}_m^t)$$
$$\text{s.t. } \|\mathbf{g}_s\|^2 \le \eta,\ s = 1, \cdots, S; \quad (45b)$$

$$\mathbf{w}_m^{t+1} := \arg\min_{\{\mathbf{w}_m\}} L_\beta(\xi^{t+1}, \mathbf{x}^{t+1}, \mathbf{g}_s^t, \eta^t, \mathbf{w}_m, \boldsymbol{\lambda}_s^t, \boldsymbol{\nu}_m^t)$$
$$\text{s.t. } d - \varepsilon_r \le \|\mathbf{w}_m\|^2 \le d + \varepsilon_r,\ m = 1, \cdots, M; \quad (45c)$$

$$\boldsymbol{\lambda}_s^{t+1} := \boldsymbol{\lambda}_s^t + \mathbf{g}_s^{t+1} - \boldsymbol{\Lambda}_s^H \mathbf{x}^{t+1},\ s = 1, \cdots, S; \quad (45d)$$

$$\boldsymbol{\nu}_m^{t+1} := \boldsymbol{\nu}_m^t + \mathbf{w}_m^{t+1} - \mathbf{A}_m^H \mathbf{x}^{t+1},\ m = 1, \cdots, M; \quad (45e)$$

Obviously, the optimization problem in (8) is split into several independently subproblems (45a)–(45e), where the subproblems (45a), (45b), and (45c) are subject to the CM constraints, quadratic inequality constraints, and double-sided constraints, respectively. Additionally, the $\mathbf{g}_s$- and $\mathbf{w}_m$-updates can be carried out independently and in parallel for each s and m, and so do $\boldsymbol{\lambda}_s$ and $\boldsymbol{\nu}_m$.

In the rest of the subsection, we will show how to solve (45a)–(45c).

1) Solution to (45a): Defining $\mathbf{A}_{M+s} = \boldsymbol{\Lambda}_s, \mathbf{w}_{M+s}^t = \mathbf{g}_s^t$, $\boldsymbol{\nu}_{M+s}^t = \boldsymbol{\lambda}_s^t$, for $s = 1, \cdots, S$, and $\mathbf{u}_p^t = \mathbf{w}_p^t + \boldsymbol{\nu}_p^t$, for $p = 1, \cdots, P$ (with $P = M + S$), and ignoring the constant terms in (45a), we simplify the optimization problem in (45a) as follows:

$$\begin{aligned}\min_{\xi,\mathbf{x}}\ & \sum_{p=1}^{P}\|\mathbf{u}_p^t - \mathbf{A}_p^H \mathbf{x}\|^2 \\ \text{s.t. } & |x(\bar{n})| = \xi\ ,\ \ \bar{n} = 1, \cdots, LN. \end{aligned} \quad (46)$$

Similar to (16), by introducing auxiliary phase vector variables $\boldsymbol{\phi} = [\phi(1), \cdots, \phi(LN)]^T$, we transform the constraints $|x(\bar{n})| = \xi$ for $\bar{n} = 1, \cdots, LN$, into $\mathbf{x} = \xi e^{j\boldsymbol{\phi}}$. Thus, we recast (46) as the following optimization problem without modulus operation

$$\min_{\xi,\boldsymbol{\phi},\mathbf{x}} \sum_{p=1}^{P}\|\mathbf{u}_p^t - \mathbf{A}_p^H \mathbf{x}\|^2 \ \text{ s.t. } \mathbf{x} = \xi e^{j\boldsymbol{\phi}}. \quad (47)$$

Then, we construct the following augmented Lagrangian (scaled form):

$$L_{\varphi}(\xi,\boldsymbol{\phi},\mathbf{x},\boldsymbol{\kappa}) = \sum_{p=1}^{P}\|\mathbf{u}_p^t - \mathbf{A}_p^H\mathbf{x}\|^2 + \frac{\varphi}{2}(\|\mathbf{x}-\xi e^{j\boldsymbol{\phi}}+\boldsymbol{\kappa}\|^2 - \|\boldsymbol{\kappa}\|^2), \quad (48)$$

where $\boldsymbol{\kappa}\in\mathbb{C}^{LN\times 1}$ is the scaled dual variable, and $\varphi>0$ is the step size. We apply the alternating direction method of multipliers to solve (46) via the following iterative steps:

$$\{\boldsymbol{\phi}^{i+1},\xi^{i+1}\} := \arg\min_{\boldsymbol{\phi},\xi} L_{\varphi}(\boldsymbol{\phi},\xi,\mathbf{x}^i,\boldsymbol{\kappa}^i), \quad (49a)$$

$$\mathbf{x}^{i+1} := \arg\min_{\mathbf{x}} L_{\varphi}(\boldsymbol{\phi}^{i+1},\xi^{i+1},\mathbf{x},\boldsymbol{\kappa}^i), \quad (49b)$$

$$\boldsymbol{\kappa}^{i+1} := \boldsymbol{\kappa}^i + \mathbf{x}^{i+1} - \xi^{i+1}e^{j\boldsymbol{\phi}^{i+1}}. \quad (49c)$$

Defining $\mathbf{b}^i = \mathbf{x}^i + \boldsymbol{\kappa}^i$, and ignoring the constant terms in (49a), we have

$$\min_{\boldsymbol{\phi},\xi} \|\mathbf{b}^i - \xi e^{j\boldsymbol{\phi}}\|^2. \quad (50)$$

Obviously, $\boldsymbol{\phi}$ is independent of ξ, and depends on only the phases of $\mathbf{b}^i$, i.e.,

$$\boldsymbol{\phi}^{i+1} = \angle\mathbf{b}^i. \quad (51)$$

Substituting (51) into (50) yields an optimization problem of a single variable ξ:

$$\|\mathbf{b}^i - \xi e^{j\boldsymbol{\phi}^{i+1}}\|^2 = \breve{a}\xi^2 + \breve{b}\xi + \breve{c}, \quad (52)$$

where $\breve{a} = LN > 0, \breve{b} = -2\sum_{l=1}^{LN}|b^i(l)| < 0$, and $\breve{c} = \|\mathbf{b}^i\|^2$. Obviously, the optimal ξ^{i+1} is given by:

$$\xi^{i+1} = -\frac{\breve{b}}{2\breve{a}}. \quad (53)$$

Defining $\hat{\mathbf{x}}^i = \xi^{i+1}e^{j\boldsymbol{\phi}^{i+1}} - \boldsymbol{\kappa}^i$ for (49b), we simplify (49b) into:

$$\min_{\mathbf{x}} \sum_{p=1}^{P}\|\mathbf{u}_p^t - \mathbf{A}_p^H\mathbf{x}\|^2 + \frac{\varphi}{2}\|\mathbf{x}-\hat{\mathbf{x}}^i\|^2. \quad (54)$$

According to Lemma 1, the solution to (54) is given by:

$$\mathbf{x}^{i+1} = \left(\mathbf{I}_N \otimes \mathbf{Z}_{\varphi}^{-1}\right)\mathbf{s}, \quad (55)$$

where $\mathbf{Z}_{\varphi} = \sum_{p=1}^{P}\mathbf{a}(\theta_p)\mathbf{a}^H(\theta_p) + \frac{\varphi}{2}\mathbf{I}_L \in \mathbb{C}^{L\times L}$, and $\mathbf{s} = \sum_{p=1}^{P}\mathbf{A}_p\mathbf{u}_p^t + \hat{\mathbf{x}}^i$.

Thus, the solving procedure for (45a) is summarized in Algorithm 3.

2) Solution to (45b): Defining $\hat{\mathbf{g}}_s^t = \boldsymbol{\Lambda}_s^H\mathbf{x}^{t+1} - \boldsymbol{\lambda}_s^t$, for $s = 1,\cdots,S$, and ignoring the constant terms in (45b), we rewrite (45b) as

$$\min_{\{\mathbf{g}_s\},\eta} \eta + \frac{\beta}{2}\sum_{s=1}^{S}\|\mathbf{g}_s - \hat{\mathbf{g}}_s^t\|^2 \quad \text{s.t. } \|\mathbf{g}_s\|^2 \le \eta, s=1,\cdots,S, \quad (56)$$

Algorithm 3: Solution to (45a).

Input: $\{\mathbf{u}_p^t\}$, step size φ, iteration stop tolerance ζ, and the maximum iteration number I.
Initialization: $\boldsymbol{\phi}^0, \boldsymbol{\kappa}^0, i = 0$.
1: **while** $\|\mathbf{x}^i - \xi^i e^{j\boldsymbol{\phi}^i}\| > \zeta$ and $i \le I$ **do**
2: Obtain $\boldsymbol{\phi}^{i+1}$ and ξ^{i+1} using (51) and (53), respectively;
3: Obtain $\mathbf{x}^{i+1}$ using (55);
4: Update $\boldsymbol{\kappa}^{i+1}$ using (49c);
5: $i = i+1$.
6: **end while**
Output: MIMO radar waveform vector $\mathbf{x}^{i+1}$.

where η is coupled with $\{\mathbf{g}_s\}$. However, when η^{t+1} is provided, (56) reduces to

$$\min_{\mathbf{g}_s} \|\mathbf{g}_s - \hat{\mathbf{g}}_s^t\|^2 \ \text{ s.t. } \|\mathbf{g}_s\|^2 \le \eta^{t+1}, \quad (57)$$

for $s = 1,\cdots,S$. According to Lemma 2, the optimal $\mathbf{g}_s^{t+1}$ is given by:

$$\mathbf{g}_s^{t+1} = \begin{cases} \sqrt{\eta^{t+1}}\frac{\hat{\mathbf{g}}_s^t}{\|\hat{\mathbf{g}}_s^t\|}, & \text{if } \|\hat{\mathbf{g}}_s^t\| > \sqrt{\eta^{t+1}}, \\ \hat{\mathbf{g}}_s^t, & \text{otherwise.} \end{cases} \quad (58)$$

Similarly, if ϑ_s is set to be null or notch with the depth ι (see Exp. 4 for details), the optimal $\mathbf{g}_s^{t+1}$ is given by

$$\mathbf{g}_s^{t+1} = \begin{cases} \sqrt{\iota}\frac{\hat{\mathbf{g}}_s^t}{\|\hat{\mathbf{g}}_s^t\|}, & \text{if } \|\hat{\mathbf{g}}_s^t\| > \sqrt{\iota}, \\ \hat{\mathbf{g}}_s^t, & \text{otherwise.} \end{cases} \quad (59)$$

Substituting (58) into (56) yields a single variable optimization problem:

$$\min_{\eta} \ p(\eta), \quad (60)$$

where $p(\eta) = \eta + \frac{\beta}{2}\sum_{s=1}^{S}\bar{w}_s(\sqrt{\eta} - \|\hat{\mathbf{g}}_s^t\|)^2$. Additionally, $\bar{w}_s = 0$ if $\|\hat{\mathbf{g}}_s^t\| < \sqrt{\eta}$; otherwise, $\bar{w}_s = 1$.

With $[u_0,u_1,\cdots,u_K]$ as the ascending order set of $[\|\hat{\mathbf{g}}_1^t\|, \|\hat{\mathbf{g}}_2^t\|,\cdots,\|\hat{\mathbf{g}}_S^t\|]$, where $K \le S$ (removing repetitions), (60) can be represented in a piecewise function as:

$$p(\eta) = \{p_k(\eta) | u_{k-1} \le \sqrt{\eta} \le u_k, k = 1,\cdots,K\}, \quad (61)$$

where $p_k(\eta) = \eta + \frac{\beta}{2}\sum_{k}^{K}(\sqrt{\eta} - u_k)^2$ is defined in the region $[u_{k-1},u_k]$.

Obviously, the kth subfunction can be written as:

$$p_k(\eta) = a_k\eta + b_k\sqrt{\eta} + c_k, \quad (62)$$

where $a_k = 1 + \frac{\beta}{2}\sum_{l=k}^{K}1$, $b_k = -\beta\sum_{l=k}^{K}u_l$, $c_k = \frac{\beta}{2}\sum_{l=k}^{K}u_l^2$, and $\sqrt{\eta}\in[u_{k-1},u_k]$. Thus, (60) is equivalent to the following optimization problem:

$$\min_{\eta}\{p_1(\eta),p_2(\eta),\cdots,p_K(\eta)\} \ \text{s.t. } u_0 \le \sqrt{\eta} \le u_K. \quad (63)$$

Obviously, the stable point of $p_k(\eta)$ is $-\frac{b_k}{2a_k}$, and the minimal value $\tilde{\eta}_k$ of the kth subfunction in the region $[u_{k-1},u_k]$ is determined from the following cases:

Case 1: if $-\frac{b_k}{2a_k} \le u_{k-1} \le u_k$, we get the optimal value at $\tilde{\eta}_k = u_{k-1}$.

Algorithm 4: WRC-design.

Input: Step size β, iteration stop tolerance $\tilde{\iota}$ and the maximum iteration number T_0, desired mainlobe level d, ripple term ε_r, mainlobe region Θ, and sidelobe region Ω.

Initialization: $\{\mathbf{y}_s^0\}, \{\mathbf{z}_m^0\}, \{\boldsymbol{\lambda}_s^0\}$ and $\{\boldsymbol{\nu}_s^0\}$, $t = 0$.

1: **while** $|\eta^{t+1} - \eta^t| > \tilde{\iota}$ and $t \leq T_0$ **do**
2: Obtain $\mathbf{x}^{t+1}$ using **Algorithm 3**;
3: Determine $\{\mathbf{g}_s^{t+1}\}$ and η^{t+1} using (58) or (59), (64), respectively; Determine $\{\mathbf{w}_m^{t+1}\}$ using (66);
4: Update $\{\boldsymbol{\lambda}_s^{t+1}\}, \{\boldsymbol{\nu}_m^{t+1}\}$ using (45d) and (45e), respectively;
5: $t = t + 1$.
6: **end while**

Output: MIMO radar probing signal $\mathbf{x}$.

Case 2: if $u_{k-1} \leq -\frac{b_k}{2a_k} \leq u_k$, we get the optimal value at $\tilde{\eta}_k = -\frac{b_k}{2a_k}$.

Case 3: if $u_{k-1} \leq u_k \leq -\frac{b_k}{2a_k}$, we get the optimal value at $\tilde{\eta}_k = u_k$.

Inserting $\tilde{\eta}_k$ into (62), we obtain the potential minimal value of the kth subfunction $p_k(\tilde{\eta}_k)$. By selecting the global minimum value from all the K locally minimal values, we obtain the optimal η^{t+1} as

$$\eta^{t+1} = \{\arg\min_{\tilde{\eta}_k}\{p_1(\tilde{\eta}_1), p_2(\tilde{\eta}_2), \cdots p_K(\tilde{\eta}_K)\}\}^2. \quad (64)$$

Once η^{t+1} is determined, the optimal $\{\mathbf{g}_s^{t+1}\}$ is computed from (58).

3) Solution to (45c): Defining $\hat{\mathbf{w}}_m^t = \mathbf{A}_m^H \mathbf{x}^{t+1} - \boldsymbol{\nu}_m^t$, for $m = 1, \cdots, M$, and ignoring the constant terms in (45c), we rewrite (45c) as

$$\min_{\mathbf{w}_m} \ \|\mathbf{w}_m - \hat{\mathbf{w}}_m^t\|^2 \text{ s.t. } d - \varepsilon_r \leq \|\mathbf{w}_m\|^2 \leq d + \varepsilon_r, \quad (65)$$

for $m = 1, \cdots, M$.

According to Lemma 2, the optimal $\mathbf{w}_m^{t+1}$ is readily given by

$$\mathbf{w}_m^{t+1} = \begin{cases} \sqrt{d+\varepsilon_r}\frac{\hat{\mathbf{w}}_m^t}{\|\hat{\mathbf{w}}_m^t\|}, & \text{if } \|\hat{\mathbf{w}}_m^t\| > \sqrt{d+\varepsilon_r}, \\ \sqrt{d-\varepsilon_r}\frac{\hat{\mathbf{w}}_m^t}{\|\hat{\mathbf{w}}_m^t\|}, & \text{if } \|\hat{\mathbf{w}}_m^t\| < \sqrt{d-\varepsilon_r}, \\ \hat{\mathbf{w}}_m^t, & \text{otherwise.} \end{cases} \quad (66)$$

Then, (45a)–(45e) are repeated until a stopping criterion is reached. The proposed WRC-design algorithm is summarized in Algorithm 4.

C. Convergence Performance Analysis

In this subsection, we discuss the convergence performance of the proposed algorithms. In general, if the optimization problem is convex, the ADMM can guarantee the global convergence [29]. However, when the problem is nonconvex, the theoretical proof of the corresponding convergence is still an open research problem [31], [32], [33]. Although the following theorems show that the sequences generated by the proposed algorithms are convergent under some mild conditions, being far from satisfactory, they still provide some assurance on the reliability of the proposed algorithms [30].

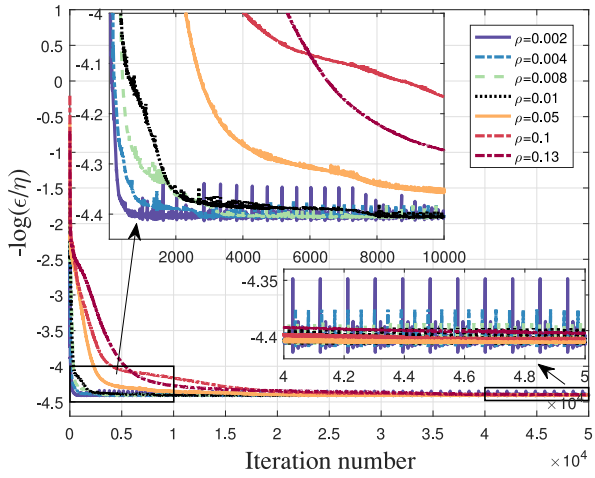

Fig. 1. Influence of the step size on the convergence of the WBM-design algorithm.

Theorem 1: [30] Let $\{\mathbf{x}^t, \mathbf{y}_s^t, \eta^t, \mathbf{z}_m^t, \boldsymbol{\lambda}_s^t, \boldsymbol{\nu}_m^t, \varepsilon^t\}$ be a sequence generated by the WBM-design steps (13a)–(13e) with $\rho > 0$. Assume that $\lim_{t\to\infty} \boldsymbol{\nu}_m^{t+1} - \boldsymbol{\nu}_m^t = \mathbf{0}$ and $\lim_{t\to\infty} \boldsymbol{\lambda}_s^{t+1} - \boldsymbol{\lambda}_s^t = \mathbf{0}$. Then there exists a limit point $\{\mathbf{x}^\star, \mathbf{y}_s^\star, \eta^\star, \mathbf{z}_m^\star, \boldsymbol{\lambda}_s^\star, \boldsymbol{\nu}_m^\star, \varepsilon^\star\}$, which is an optimal solution to (11).

Proof: See Appendix C.

Theorem 2: [30] Let $\{\xi^t, \mathbf{x}^t, \mathbf{g}_s^t, \eta^t, \mathbf{w}_m^t, \boldsymbol{\lambda}_s^t, \boldsymbol{\nu}_m^t\}$ be a sequence generated by the WRC-design steps (45a)–(45e) with $\beta > 0$. Assume that $\lim_{t\to\infty} \boldsymbol{\nu}_m^{t+1} - \boldsymbol{\nu}_m^t = \mathbf{0}$ and $\lim_{t\to\infty} \boldsymbol{\lambda}_s^{t+1} - \boldsymbol{\lambda}_s^t = \mathbf{0}$. Then there exists a limit point $\{\xi^\star, \mathbf{x}^\star, \mathbf{g}_s^\star, \eta^\star, \mathbf{w}_m^\star, \boldsymbol{\lambda}_s^\star, \boldsymbol{\nu}_m^\star\}$, which is an optimal solution to (43).

Proof: The proof can be obtained by using the same technique discussed in Appendix C.

In addition, the following theorem shows that the Algorithm 3 can converge to the set of stationary solutions [32], [33].

Theorem 3: [32], [33] For $\varphi > 2\sqrt{2}\|\sum_{p=1}^P \mathbf{A}_p \mathbf{A}_p^H\|_F$, the sequence $\mathbf{x}^i, \xi^i, \boldsymbol{\phi}^i, \boldsymbol{\kappa}^i$ generated by Algorithm 3 has the following properties

1) Dual variable is bounded by primal variable, that is, $\|\boldsymbol{\kappa}^{i+1} - \boldsymbol{\kappa}^i\| \leq \frac{2}{\varphi}\|\sum_{p=1}^P \mathbf{A}_p \mathbf{A}_p^H\|_F \|\mathbf{x}^{i+1} - \mathbf{x}^i\|$;
2) The augmented Lagrangian L_φ is descent during the $\{\mathbf{x}^i, \xi^i, \boldsymbol{\phi}^i, \boldsymbol{\kappa}^i\}$ update;
3) The augmented Lagrangian $L_\varphi(\mathbf{x}^i, \xi^i, \boldsymbol{\phi}^i, \boldsymbol{\kappa}^i)$ is lower bounded for all i and converges as $i \to \infty$;
4) $\lim_{i\to\infty} \|\mathbf{x}^i - \xi^i e^{j\boldsymbol{\phi}^i}\| = 0$;
5) Let $\{\mathbf{x}^\star, \xi^\star, \boldsymbol{\phi}^\star, \boldsymbol{\kappa}^\star\}$ denotes any limit point of the sequence $\{\mathbf{x}^{i+1}, \xi^{i+1}, \boldsymbol{\phi}^{i+1}, \boldsymbol{\kappa}^{i+1}\}$ generated by Algorithm 3. Then the following statements hold

$$\mathbf{0} \in \nabla f(\mathbf{x}^\star) + \varphi\boldsymbol{\gamma}^\star,$$
$$\mathbf{x}^\star = \xi^\star \boldsymbol{\phi}^\star. \quad (67)$$

That is, any limit point of Algorithm 3 is a stationary solution to (46).

Proof: See Appendix D.

Note that when $\xi = 1$, Algorithm 3 reduces to Algorithm 1, thus Theorem 3 is also applicable to Algorithm 1.

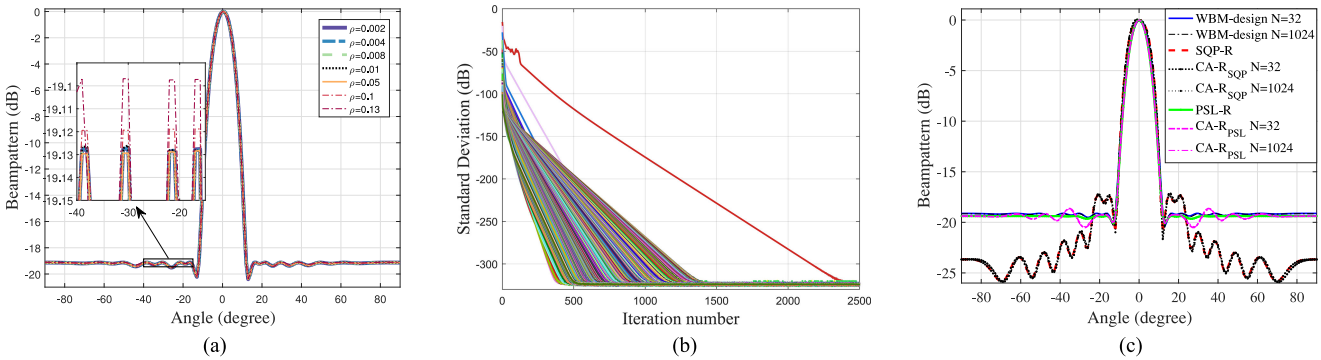

Fig. 2. (a) Beampattern results obtained by using different step sizes in Exp. 1; (b) Standard deviation of waveform modulus versus number of inner iterations; (c) Normalized focus pattern design results in Exp. 1.

D. Computational Complexity Analysis

In this subsection, we discuss the computational complexity of the proposed algorithms. From Algorithm 1 (corresponding to the first update step of the WBM-design (13a)), we can see that the computational complexity is dominated by the matrix inversion, which requires $\mathcal{O}(L^{2.373})$ [27], and matrix-to-vector multiplications at every iteration. Thus, the overall computational complexity of Algorithm 1 is $\mathcal{O}(L^{2.373}+(I+P)NL)$, where I is the total number of inner iterations. The rest of the update steps of the WBM-design (see (13b)–(13e)) yields a simple closed form solution and only requires basic matrix-to-vector multiplications, and thus the computational complexity of these steps is $\mathcal{O}(T_0NLP+T_0NP)$, where T_0 is the total number of iterations. To sum up, the over all computational complexity of the WBM-design algorithm is $\mathcal{O}(L^{2.373}+T_0NL(I+2P)+T_0NP)$. Similarly, Algorithm 3 (solving (45a)) takes also $\mathcal{O}(L^{2.373}+(I+P)NL)$, and the rest of the steps of the WRC-design (see (45b)–(45e)) are the same as the WBM-design (see (13b)–(13e)). Therefore, the overall computational complexity of the WRC-design is also $\mathcal{O}(L^{2.373}+T_0NL(I+2P)+T_0NP)$.

The counterparts discussed in [2], [12] and [18] for covariance matrix (which are compared in the numerical example section) need to solve the semidefinite programming (SDP), and their computational complexities are all $\mathcal{O}(L^{3.5})$ (only with regard to number of antennas L). Moreover, the computational complexity of CA for waveform set [14] is $\mathcal{O}(T_0(3L^2N+N^3))$. Thus, the over all computational complexities of the two-step methods in [2], [12], [18] and [14] are all $\mathcal{O}(L^{3.5}+T_0(3L^2N+N^3))$, which implies that our methods have comparable computational burden, especially for large-scale CM waveform design.

IV. Numerical Examples

In this section, computer simulations are conducted to assess the performance of the proposed algorithms. In all experiments we consider, unless stated otherwise, a uniform linear array of $L=16$ sensors with half-wavelength element spacing, and each transmit signal pulse consists of $N=32$ samples. Stop criteria $\zeta=10^{-8}$ and maximum number of iteration $I=500$ are applied to update $\mathbf{x}$. And the maximum iteration number $T_0=5000$ is set for Algorithms 2 and 4. Other parameters, such as scaled dual variables and auxiliary variables, are initialized in a random manner. In addition, the spatial angle region $[-90^\circ,90^\circ]$ is divided into $V=181$ angle grids with uniform angle interval 1°.

TABLE I
Comparison of Runtimes (seconds) in Exp. 1

Method	WBM	PSL-R	CA-$\mathbf{R}_{PSL}$	SQP-R	CA-$\mathbf{R}_{SQP}$
$N=32$	22.73	2.23	2.97	2.30	3.09
$N=1024$	89.56	2.23	170.16	2.30	175.26

A. Test on WBM-Design

In this subsection, experiments are conducted to testify the performance of the proposed WBM-design algorithm. For comparison purposes, we consider the counterparts, i.e., the Semi-Definite Quadratic Programming (SQP) based minimum sidelobe beampattern design method [2] to design the covariance matrix (named SQP-$\mathbf{R}$), PSL oriented design method [18] for optimal covariance matrix (named PSL-$\mathbf{R}$, which can be used as a benchmark for the minimum PSL based design method), and the cyclic algorithm (CA) [14] to generate the CM waveform set from the obtained covariance matrix (named CA-$\mathbf{R}_{SQP}$ and CA-$\mathbf{R}_{PSL}$, respectively).

Experiment 1: Convergence Performance and CM Property. In this experiment, we explore the convergence performance of the WBM-design algorithm and the CM property of the obtained waveform vector $\mathbf{x}$. Here we consider a narrow focused beam, where the mainlobe point $\theta_0=0^\circ$, and the region of sidelobe is $\Omega\in[-90^\circ,-12^\circ]\cup[12^\circ,90^\circ]$.

In the first, we testify the influence of the step size on the convergence of the WBM-design algorithm. In Fig. 1, we plot the curves of the objective value $-\log(\frac{\varepsilon}{\eta})$ with different step sizes ρ. From the figure we can see that the WBM-design algorithm with the smaller step size (e.g., $\rho=0.002$) converges faster than that with the larger step size (e.g., $\rho=0.13$), while too small step size (e.g., $\rho=0.002$) will result in a slightly oscillation (about 0.05) of the objective function values as the iterative process goes on. In addition, this oscillation is diminishing with the increasing of step size. Practically, however, these oscillations have little effect on our design. As shown in Fig. 2(a), the difference among the beampattern results obtained with different step sizes (mainlobe peak is normalized to 0 dB) is only about

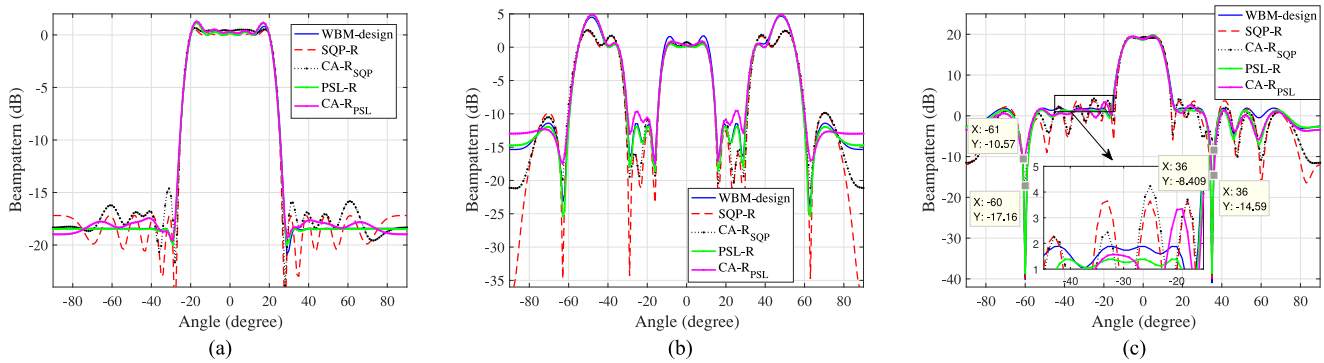

Fig. 3. (a) Normalized wide mainlobe pattern design results in Exp. 2; (b) Normalized multi-beam pattern design results in Exp. 3; (c) Notch pattern design results in Exp. 4.

0.03 dB in PSL, which may be neglected. On account of the rate of convergence and stability of the proposed algorithm, we set step size $\rho = 0.01$ in the following experiments.

Next, we evaluate the CM property of the waveform vector $\mathbf{x}$ obtained by Algorithm 1. In this experiment, stop criteria $\zeta = 0$, maximum iteration number $I = 2500$ and the step size $\alpha = 200$ (which is chosen according to the Theorem 3) are applied to update $\mathbf{x}$, and other parameters remain unchanged. For the tth $\mathbf{x}$-update step (the tth call of Algorithm 1), we compute the standard deviation value of the waveform modulus $|\mathbf{x}|$ at the ith inner iteration, denoted by $\Delta^t(i)$ (where $\mathbf{\Delta}^t \in \mathbb{R}^I$), i.e., $\Delta^t(i) = \text{std}\left(|\mathbf{x}^i|\right),\ t = 1, \cdots, T_0,\ i = 1, \cdots, I$, and plot the dB version of the $\{\mathbf{\Delta}^t\}_{t=1}^{T_0}$ in Fig. 2(b). From the figure we can see that Algorithm 1 always returns a CM waveform vector $\mathbf{x}$ (the standard deviation of the waveform modulus $\Delta^t(i)$ tends to zero as the iteration number i increases), which implies that the obtained waveform vector $\mathbf{x}$ is always of the CM property.

Finally, the dB version of the normalized beampattern synthesis results (with lengths $N = 32, 1024$), WBM-desing (with $\rho = 0.01$), $\mathbf{R}_{SQP}$, CA-$\mathbf{R}_{SQP}$, $\mathbf{R}_{PSL}$ and CA-$\mathbf{R}_{PSL}$ are plotted in Fig. 2(c). Furthermore, the runtimes of the five algorithms are provided in Table I. From the figure we can see that the beampattern obtained by the proposed WBM-design algorithm is almost the same as that using the optimal $\mathbf{R}_{PSL}$, and also has lower PSL in comparison to that using waveform set obtained by CA (CA-$\mathbf{R}_{SQP}$ and CA-$\mathbf{R}_{PSL}$). In addition, the results in Table I show that when designing a long code (e.g., $N = 1024$), the runtimes for computing covariance matrices ($\mathbf{R}_{PSL}$ and $\mathbf{R}_{SQP}$) remain the same. Whereas, the runtime of CA for waveform set increases dramatically. Comparatively, the runtime of the WBM-design algorithm does not change significantly and is lower than that of CA-$\mathbf{R}_{SQP}$ and CA-$\mathbf{R}_{PSL}$. All those imply that the proposed algorithm is also applicable to large-scale CM waveform design. Especially, the WBM-design algorithm can synthesize CM waveform directly, rather than two-step strategy proposed in [2] and [18]. In the following experiments, the step size $\alpha = 200$ is set.

Experiment 2: Wide Mainlobe Pattern Design. When the colocated MIMO radar works in a search mode, a wide radiation beam is desired to illuminate the region of interest uniformly [22]. Hence, in this experiment, we consider designing a wide beam with the mainlobe region $\Theta \in [-20^\circ, 20^\circ]$ and the sidelobe region $\Omega \in [-90^\circ, -28^\circ] \cup [28^\circ, 90^\circ]$. It can be seen from the synthesized results in Fig. 3(a) that the WBM-design method generates lower PSL of beampatterns and is almost the same as the result obtained by the optimal $\mathbf{R}_{PSL}$, whereas both CA-$\mathbf{R}_{SQP}$ and CA-$\mathbf{R}_{PSL}$ suffer from high PSL.

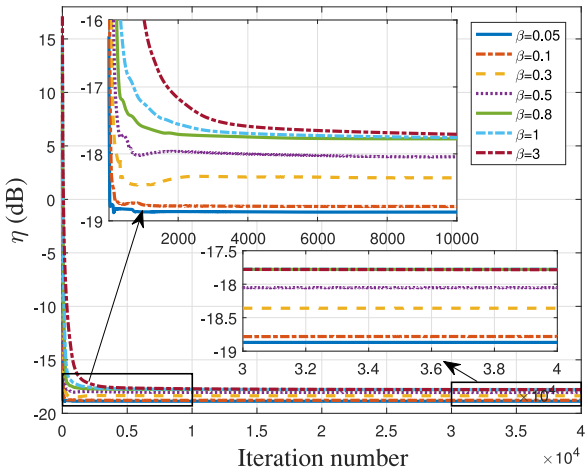

Fig. 4. Influence of the step size on the convergence of the WRC-design algorithm.

Experiment 3: Multi-Beam Pattern Design. When the directions of the potential targets are known inaccurately, multiple beams are needed to make the MIMO radar system work in the tracking mode of multiple targets [22]. Here we implement such a scenario in Experiment 3, where three beams (mainlobe) are $[-55^\circ, -35^\circ], [-10^\circ, 10^\circ]$, and $[35^\circ, 55^\circ]$, and the sidelobe regions are $\Omega \in [-90^\circ, -51^\circ] \cup [-29^\circ, -16^\circ] \cup [16^\circ, 29^\circ] \cup [51^\circ, 90^\circ]$. It can be observed from Fig. 3(b) that the beampattern obtained by the WBM-design algorithm is very close to that using the optimal $\mathbf{R}_{PSL}$. Comparatively, the beampatterns obtained by the CA-$\mathbf{R}_{SQP}$ and CA-$\mathbf{R}_{PSL}$ suffer from higher PSL because the approximation error exists in the two-step strategy.

Experiment 4: Notch Pattern Design. To achieve synthesized beampattern with a null or notch to suppress the signal-dependent interference [14] at the angular locations $\{\vartheta_{\bar{s}}\}_{\bar{s}=1}^{\bar{S}}$, the following constraints

$$\mathbf{x}^H \mathbf{A}(\vartheta_{\bar{s}}) \mathbf{A}^H(\vartheta_{\bar{s}}) \mathbf{x} \le \iota, \bar{s} = 1, \cdots, \bar{S}, \tag{68}$$

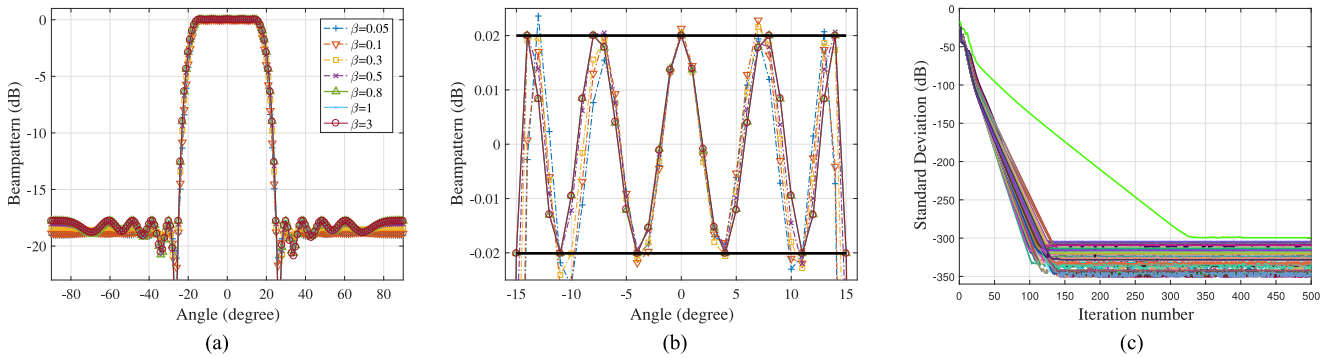

Fig. 5. (a) Beampattern results obtained by using different step sizes in Exp. 5; (b) Zoomed mainlobe of Fig. 5(a); (c) Standard deviation of waveform modulus versus number of inner iterations in Exp. 5.

are appended to the constraints in (6) (and also (8)), where ι is the prespecified null depth (the obtained problem can be solved by Algorithm 2 or 4 efficiently). Here we consider a beampattern with two -40 dB nulls at $\vartheta_1 = -60°$, $\vartheta_2 = 35°$. The mainlobe and sidelobe regions are $[-8°, 8°]$ and $[-90°, -17°] \cup [17°, 90°]$, respectively. In Fig. 3(c), we show the unnormalized results to check the attained null depth. It is easily found that the WBM-design method attains the predetermined null depth. However, the null levels obtained by the waveform set CA-$\mathbf{R}_{SQP}$ are -17.160 dB and -8.409 dB, and those of CA-$\mathbf{R}_{PSL}$ are -10.570 dB and -14.590 dB, which are higher than the desired null levels. Additionally, it can be observed from Fig. 3(c) that the beampattern obtained by the WBM-design method can achieve lower PSL than that of the SQP-based algorithm.

From Figs. 2(c)–3(c), some observations can be concluded as follows: 1) by comparing the synthesized results, it is easily found that there exist nonnegligible approximation errors in the two-step methods; 2) the beampattern obtained by the proposed WBM-design method can well approximate the beampattern obtained by the optimal covariance matrix $\mathbf{R}_{PSL}$ in [18]; 3) among the investigated (CA-$\mathbf{R}_{SQP}$ and CA-$\mathbf{R}_{PSL}$) schemes, the proposed one is the best in terms of deep null and PSL; 4) in terms of complexity requirement, the proposed method is the most attractive for large-scale CM waveform design.

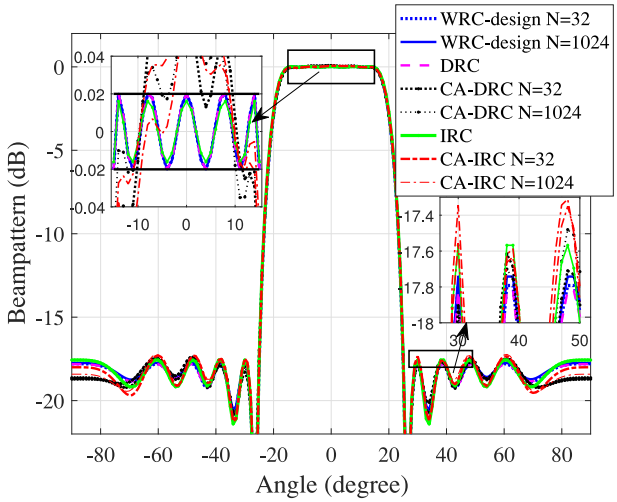

Fig. 6. Wide mainlobe pattern design results in Exp. 5.

TABLE II
COMPARISON OF RUNTIMES (SECONDS) IN EXP. 5

Method	WRC	DRC	CA-DRC	IRC	CA-IRC
$N = 32$	5.58	5.41	5.67	5.10	5.47
$N = 1024$	65.68	5.41	99.03	5.10	101.24

B. Test on WRC-Design

In this subsection, we investigate the performance of the proposed WRC-design algorithm. For comparison purposes, we simultaneously implement two important ripple control methods, i.e., the Indirect Ripple Control (IRC) and Direct Ripple Control (DRC) methods (which are obtained by the convex optimization technique SDP, and the covariance matrix obtained by DRC method can be used as a benchmark for our WRC-design method) [12], to obtain the corresponding covariance matrices. Additionally, the obtained CM waveform sets from the covariance matrices via CA are also used for comparisons, named as CA_IRC and CA_DRC. For the focused beampattern design, there is no ripple constraint for a single mainlobe location, and thus we have not considered the focused beampattern design problem in this subsection.

Experiment 5: Convergence Performance and CM Property. In the experiment, we consider the wide mainlobe beampattern design problem, where the mainlobe and sidelobe regions are $\Theta \in [-15°, 15°]$, and $\Omega \in [-90°, -26°] \bigcup [26°, 90°]$, respectively. In addition, $d = 0$ dB and $\varepsilon_r = 0.02$ dB are set.

In the first, we discuss the convergence performance of the WRC-design algorithm under the different choices of step size. The objective values with different step sizes are compared in Fig. 4. Moreover, the obtained beampattern results with different step sizes are shown in Figs. 5(a) and (b) (enlarged mainlobe region). The results show that the WRC-design algorithm converges faster if a small step size is set. However, the WRC-design algorithm with too small step size (e.g., $\beta \leq 0.5$) fails to meet the ripple constraint requirement, as shown in Fig. 5(b). Obviously, $\beta \geq 0.8$ is a proper choice for the WRC-design algorithm.

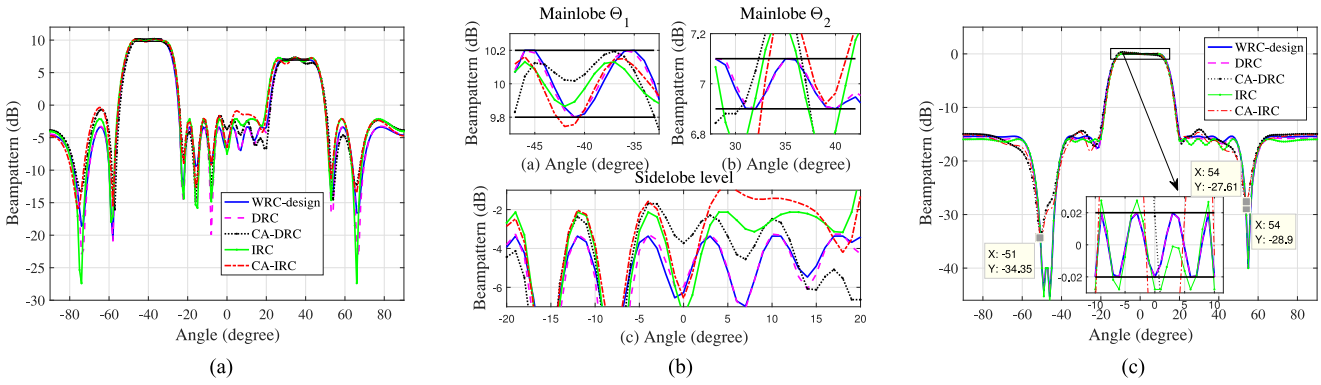

Fig. 7. (a) Multi-beam pattern design results in Exp. 6; (b) Zoomed mainlobe and sidelobe subregions in Exp. 6; (c) Null pattern design results in Exp. 7.

Next, we analyze the CM property of the obtained waveform vector $\mathbf{x}$. The step size $\varphi = 200$ (which is chosen according to the Theorem 3), the maximum iteration number $I = 500$ and the stop criteria $\zeta = 0$ are set for Algorithm 3, and other parameters remain the same. Similar to Experiment 1, we compute the standard deviation values $\{\mathbf{\Delta}\}_{t=1}^{T_0}$ and plot them in Fig. 5(c) (in dB), from which we can see that the obtained waveform tends to be unimodular after 350 inner iterations.

Finally, Fig. 6 shows the beampattern synthesis results (with different code lengths) obtained by the WRC-design (with $\beta = 0.8$), IRC, DRC, CA-DRC and CA-IRC. For comparison purposes, the enlarged mainlobe region and local sidelobe region are also plotted in the blank space of Fig. 6. Furthermore, the runtimes of the investigated schemes are provided in Table II. From Fig. 6, we can observe that the proposed WRC-design method can precisely control the mainlobe ripple, and so does DRC. Whereas, the waveform set obtained by CA (CA-DRC and CA-IRC) fails to achieve the ripple requirements and also suffers from higher PSL due to the approximation error. In addition, the result in Table II shows that the difference of computational time among the WRC-design, CA-DRC and CA-IRC are insignificant for $N = 32$. However, for the large-scale CM waveform design problems (e.g., $N = 1024$), the proposed method is much faster than the two-step based methods (CA-DRC and CA-IRC).

In the following experiments the step size $\beta = 0.8$ and $\varphi = 200$ are set.

Experiment 6: Multi-Beam Pattern Design. In some scenarios, targets of interest may have different radar cross section (RCS). MIMO radar systems need to transmit more radiation power to the directions of the small RCS targets to have the same detection capability for different targets [22]. Consequently, we consider the multi-beam pattern design problem, where two mainlobe regions are $\Theta_1 \in [-48^\circ, -32^\circ]$ and $\Theta_2 \in [27^\circ, 43^\circ]$, respectively; moreover, the sidelobe regions are $\Omega \in [-90^\circ, -56^\circ] \cup [-24^\circ, 19^\circ] \cup [51^\circ, 90^\circ]$. In addition, the ripple parameters of the two mainlobe subregions are $\{d_1 = 10$ dB$, \varepsilon_1 = 0.2$ dB$\}$, and $\{d_2 = 7$ dB$, \varepsilon_2 = 0.1$ dB$\}$. The synthesized results are plotted in Fig. 7(a), and the enlarged mainlobe regions (Θ_1, Θ_2) and sidelobe subregions $([-20^\circ, 20^\circ])$ are plotted in Fig. 7(b). From the two figures, we can see that: i) although the obtained covariance matrices (DRC) meet with the ripple constraints accurately, the obtained waveforms (CA-DRC) from the covariance matrices no longer meet with the ripple constraints; and ii) just similar to the DRC method, the proposed WRC-design method can precisely control both the sidelobe levels and the mainlobe ripple term.

Experiment 7: Null Pattern Design. In this experiment, we consider a null pattern design problem, where there is a -40 dB null at $\vartheta_1 = 55^\circ$ and a -40 dB null region at $\bar{\Omega} \in [-50^\circ, -45^\circ]$. Additionally, the mainlobe and sidelobe regions are $[-10^\circ, 10^\circ]$ and $[-90^\circ, -21^\circ] \bigcup [21^\circ, 90^\circ]$, respectively. In addition, $d = 0$ dB and $\varepsilon = 0.02$ dB are set. From the results plotted in Fig. 7(c), it is seen that the beampattern levels obtained by the WRC-design method are very close to those of DRC. However, it must be pointed out that the beampattern levels of the obtained waveforms (CA-DRC and CA-IRC) from the covariance matrix (DRC and IRC) no longer meet with the ripple constraint and suffer from high null depths, i.e., -34.35 dB and -28.90 dB.

V. Conclusion

In this paper, we have presented two new design methods to achieve the MPSTB under the CM constraints. One need not specify the pattern masks; whereas another can control the beampattern levels of interested regions precisely under the mainlobe ripple constraints. In the methods, we simplify the formulated QFP problem via decoupling the numerator and denominator, and convert the coupled double-sided quadratic constraints on the same vector variables into those on different auxiliary variables. Numerical examples show that the proposed algorithms have an advantage over several existing two-step based methods in terms of low PSL, ripple control and deep null.

Appendix

A. Proof of Lemma 1

Proof: Setting the first derivative of (21) with respect to $\mathbf{x}$ as zero yields the solution as:

$$\mathbf{x} = \mathbf{B}^{-1}\mathbf{q}, \tag{69}$$

where $\mathbf{B} = \sum_{p=1}^{P} \mathbf{A}_p \mathbf{A}_p^H + \frac{\alpha}{2}\mathbf{I}_{LN}$.

According to the property of Kronecker product (i.e., $(\mathbf{A} \otimes \mathbf{Q})(\mathbf{C} \otimes \mathbf{D}) = (\mathbf{AC}) \otimes (\mathbf{QD})$, $\mathbf{A} \otimes (\mathbf{Q} \pm \mathbf{C}) = \mathbf{A} \otimes$

$\mathbf{Q} \pm \mathbf{A} \otimes \mathbf{C}$, $(\mathbf{A} \otimes \mathbf{Q})^{-1} = \mathbf{A}^{-1} \otimes \mathbf{Q}^{-1}$, and $\frac{\alpha}{2}\mathbf{I}_{LN} = \mathbf{I}_N \otimes \frac{\alpha}{2}\mathbf{I}_L)$ [42], we have

$$\begin{aligned}\mathbf{B} &= \sum_{p=1}^{P}\left(\left(\mathbf{I}_N \otimes \mathbf{a}(\theta_p)\right)\left(\mathbf{I}_N \otimes \mathbf{a}(\theta_p)\right)^H\right) + \mathbf{I}_N \otimes \frac{\alpha}{2}\mathbf{I}_L \\ &= \mathbf{I}_N \otimes \sum_{p=1}^{P}\left(\mathbf{a}(\theta_p)\mathbf{a}^H(\theta_p)\right) + \mathbf{I}_N \otimes \frac{\alpha}{2}\mathbf{I}_L \\ &= \mathbf{I}_N \otimes \left(\sum_{p=1}^{P}\left(\mathbf{a}(\theta_p)\mathbf{a}^H(\theta_p)\right) + \frac{\alpha}{2}\mathbf{I}_L\right) \\ &= \mathbf{I}_N \otimes \mathbf{Z}_\alpha, \end{aligned} \tag{70}$$

and $\mathbf{B}^{-1} = \mathbf{I}_N \otimes \mathbf{Z}_\alpha^{-1}$. This completes the proof. ■

B. Proof of Lemma 2

Proof: We rewrite the objective function in (24) as

$$\|\mathbf{y}_s - \hat{\mathbf{y}}_s^t\|^2 = \|\mathbf{y}_s\|^2 - 2\|\mathbf{y}_s\|\|\hat{\mathbf{y}}_s^t\|\mathrm{Re}\left\langle \frac{\mathbf{y}_s}{\|\mathbf{y}_s\|}, \frac{\hat{\mathbf{y}}_s^t}{\|\hat{\mathbf{y}}_s^t\|}\right\rangle + \|\hat{\mathbf{y}}_s^t\|^2. \tag{71}$$

According to the inner product of the vectors, the maximizer with respect to $\frac{\mathbf{y}_s}{\|\mathbf{y}_s\|}$ of $\mathrm{Re}\langle \frac{\mathbf{y}_s}{\|\mathbf{y}_s\|}, \frac{\hat{\mathbf{y}}_s^t}{\|\hat{\mathbf{y}}_s^t\|}\rangle$ is given by [43]

$$\frac{\mathbf{y}_s}{\|\mathbf{y}_s\|} = \frac{\hat{\mathbf{y}}_s^t}{\|\hat{\mathbf{y}}_s^t\|}. \tag{72}$$

Substituting (72) into (71), we have

$$\|\mathbf{y}_s - \hat{\mathbf{y}}_s^t\|^2 = \|\mathbf{y}_s\|^2 - 2\|\mathbf{y}_s\|\|\hat{\mathbf{y}}_s^t\| + \|\hat{\mathbf{y}}_s^t\|^2. \tag{73}$$

With the constraint $\|\mathbf{y}_s\|^2 \le \eta^{t+1}$, (24) is equivalent to

$$\min_{\|\mathbf{y}_s\|} \left(\|\mathbf{y}_s\| - \|\hat{\mathbf{y}}_s^t\|\right)^2 \quad \text{s.t. } 0 < \|\mathbf{y}_s\| \le \sqrt{\eta^{t+1}}. \tag{74}$$

Obviously, if $\|\hat{\mathbf{y}}_s^t\| > \sqrt{\eta^{t+1}}$, then $\|\mathbf{y}_s\| = \sqrt{\eta^{t+1}}$; otherwise $\|\mathbf{y}_s\| = \|\hat{\mathbf{y}}_s^t\|$. With (72), (25) is got.

This completes the proof. ■

C. Proof of Theorem 1 [30]

Proof: Since $\lim_{t\to\infty} \boldsymbol{\nu}_m^{t+1} - \boldsymbol{\nu}_m^t = \mathbf{0}$, $\lim_{t\to\infty} \boldsymbol{\lambda}_s^{t+1} - \boldsymbol{\lambda}_s^t = \mathbf{0}$ and $\rho > 0$, from (13d)–(13e), we get the following results

$$\begin{aligned}&\lim_{t\to\infty} \mathbf{y}_s^{t+1} - \boldsymbol{\Lambda}_s^H \mathbf{x}^{t+1} = \mathbf{0}, s = 1, \cdots, S, \\ &\lim_{t\to\infty} \mathbf{z}_m^{t+1} - \mathbf{A}_m^H \mathbf{x}^{t+1} = \mathbf{0}, m = 1, \cdots, M. \end{aligned} \tag{75}$$

Moreover, since $\mathbf{x}$ is under the constant modulus constraint, which is bounded and closed set, the sequence $\{\mathbf{x}^t\}$ generated by (13a) is bounded, and there exists a stationary point $\mathbf{x}^\star$ such that $\lim_{t\to\infty} \mathbf{x}^t = \mathbf{x}^\star$. It follows from (75), the boundedness of $\{\mathbf{x}^t\}$ and the inequality

$$\begin{aligned}&\|\mathbf{y}_s^t\| \le \|\mathbf{y}_s^t - \boldsymbol{\Lambda}_s^H \mathbf{x}^t\| + \|\boldsymbol{\Lambda}_s^H \mathbf{x}^t\|, s = 1, \cdots, S, \\ &\|\mathbf{z}_m^t\| \le \|\mathbf{z}_m^t - \mathbf{A}_m^H \mathbf{x}^t\| + \|\mathbf{A}_m^H \mathbf{x}^t\|, m = 1, \cdots, M, \end{aligned} \tag{76}$$

that the sequences $\{\mathbf{y}_s^t\}$, $\{\mathbf{z}_m^t\}$ are also bounded. Therefore, there exists a stationary point $\{(\mathbf{y}_s^\star, \mathbf{z}_m^\star, \mathbf{x}^\star)\}$ such that

$$\lim_{t\to\infty}\{(\mathbf{y}_s^t, \mathbf{z}_m^t, \mathbf{x}^t)\} = \{(\mathbf{y}_s^\star, \mathbf{z}_m^\star, \mathbf{x}^\star)\}. \tag{77}$$

In addition, it follows from (13b), (13c) and (77) that the sequences $\{\eta^t\}$ and $\{\varepsilon^t\}$ are also bounded. And there exist stationary points $\eta^\star$ and $\varepsilon^\star$ such that $\lim_{t\to\infty} \eta^t = \eta^\star$ and $\lim_{t\to\infty} \varepsilon^t = \varepsilon^\star$, respectively. Thus, we have

$$\begin{aligned}&\mathbf{0} = \lim_{t\to\infty} \mathbf{y}_s^t - \boldsymbol{\Lambda}_s^H \mathbf{x}^t = \mathbf{y}_s^\star - \boldsymbol{\Lambda}_s^H \mathbf{x}^\star, s = 1, \cdots, S, \\ &\mathbf{0} = \lim_{t\to\infty} \mathbf{z}_m^t - \mathbf{A}_m^H \mathbf{x}^t = \mathbf{z}_m^\star - \mathbf{A}_m^H \mathbf{x}^\star, m = 1, \cdots, M. \end{aligned} \tag{78}$$

The proof is complete. ■

D. Proof of Theorem 3 [32]

Proof: Part 1. From the $\mathbf{x}$-update step in (49b) and $\boldsymbol{\kappa}$-update step in (49c), we have the following optimality condition

$$\begin{aligned}\mathbf{0} &= \nabla_{\mathbf{x}} L_\varphi(\boldsymbol{\phi}^{i+1}, \xi^{i+1}, \mathbf{x}^{i+1}, \boldsymbol{\kappa}^i) \\ &= \nabla f(\mathbf{x}^{i+1}) + \varphi\left(\mathbf{x}^{i+1} - \xi^{i+1} e^{j\boldsymbol{\phi}^{i+1}} + \boldsymbol{\kappa}^i\right) \\ &= \nabla f(\mathbf{x}^{i+1}) + \varphi\boldsymbol{\kappa}^{i+1}, \end{aligned} \tag{79}$$

where $f(\mathbf{x}) = \sum_{p=1}^{P} \|\mathbf{u}_p^t - \mathbf{A}_p^H \mathbf{x}\|^2$. In addition

$$\begin{aligned}&\|\nabla f(\mathbf{x}^{i+1}) - \nabla f(\mathbf{x}^i)\| \\ &= \left\| 2\sum_{p=1}^{P} \mathbf{A}_p \mathbf{A}_p^H \mathbf{x}^{i+1} - 2\sum_{p=1}^{P} \mathbf{A}_p \mathbf{A}_p^H \mathbf{x}^i \right\| \\ &\le 2\left\| \sum_{p=1}^{P} \mathbf{A}_p \mathbf{A}_p^H \right\|_F \left\| \mathbf{x}^{i+1} - \mathbf{x}^i \right\|. \end{aligned} \tag{80}$$

It follows from (79) and (80) that

$$\boldsymbol{\kappa}^{i+1} = -\frac{1}{\varphi}\nabla f(\mathbf{x}^{i+1}), \tag{81}$$

and

$$\begin{aligned}\|\boldsymbol{\kappa}^{i+1} - \boldsymbol{\kappa}^i\| &= \frac{1}{\varphi}\|\nabla f(\mathbf{x}^{i+1}) - \nabla f(\mathbf{x}^i)\| \\ &\le \frac{2}{\varphi}\left\| \sum_{p=1}^{P} \mathbf{A}_p \mathbf{A}_p^H \right\|_F \left\| \mathbf{x}^{i+1} - \mathbf{x}^i \right\|. \end{aligned} \tag{82}$$

Part 2. The difference of the augmented Lagrangian can be split into

$$\begin{aligned}&L_\varphi(\mathbf{x}^{i+1}, \xi^{i+1}, \boldsymbol{\phi}^{i+1}, \boldsymbol{\kappa}^{i+1}) - L_\varphi(\mathbf{x}^i, \xi^i, \boldsymbol{\phi}^i, \boldsymbol{\kappa}^i) \\ &= L_\varphi(\mathbf{x}^i, \xi^{i+1}, \boldsymbol{\phi}^{i+1}, \boldsymbol{\kappa}^i) - L_\varphi(\mathbf{x}^i, \xi^i, \boldsymbol{\phi}^i, \boldsymbol{\kappa}^i) \\ &+ L_\varphi(\mathbf{x}^{i+1}, \xi^{i+1}, \boldsymbol{\phi}^{i+1}, \boldsymbol{\kappa}^{i+1}) - L_\varphi(\mathbf{x}^{i+1}, \xi^{i+1}, \boldsymbol{\phi}^{i+1}, \boldsymbol{\kappa}^i) \\ &+ L_\varphi(\mathbf{x}^{i+1}, \xi^{i+1}, \boldsymbol{\phi}^{i+1}, \boldsymbol{\kappa}^i) - L_\varphi(\mathbf{x}^i, \xi^{i+1}, \boldsymbol{\phi}^{i+1}, \boldsymbol{\kappa}^i). \end{aligned} \tag{83}$$

The dual variable update step can be bounded by

$$\begin{aligned}
&L_\varphi(\mathbf{x}^{i+1},\xi^{i+1},\boldsymbol{\phi}^{i+1},\boldsymbol{\kappa}^{i+1})-L_\varphi(\mathbf{x}^{i+1},\xi^{i+1},\boldsymbol{\phi}^{i+1},\boldsymbol{\kappa}^{i})\\
&=\varphi\mathrm{Re}\left[\left(\boldsymbol{\kappa}^{i+1}-\boldsymbol{\kappa}^{i}\right)^H\left(\mathbf{x}^{i+1}-\xi^{i+1}e^{j\boldsymbol{\phi}^{i+1}}\right)\right]\\
&\overset{(a)}{=}\varphi\|\boldsymbol{\kappa}^{i+1}-\boldsymbol{\kappa}^{i}\|^2\\
&\overset{(b)}{\leq}\frac{4}{\varphi}\left\|\sum_{p=1}^{P}\mathbf{A}_p\mathbf{A}_p^H\right\|_F^2\|\mathbf{x}^{i+1}-\mathbf{x}^{i}\|^2,
\end{aligned}\tag{84}$$

where (a) and (b) are obtained by (49c) and (82), respectively. Updating $\boldsymbol{\phi}$ and ξ in (49a) yields

$$L_\varphi(\mathbf{x}^{i},\xi^{i+1},\boldsymbol{\phi}^{i+1},\boldsymbol{\kappa}^{i})-L_\varphi(\mathbf{x}^{i},\xi^{i},\boldsymbol{\phi}^{i},\boldsymbol{\kappa}^{i})\leq 0.\tag{85}$$

The third term in (83) is bounded by

$$\begin{aligned}
&L_\varphi(\mathbf{x}^{i+1},\xi^{i+1},\boldsymbol{\phi}^{i+1},\boldsymbol{\kappa}^{i})-L_\varphi(\mathbf{x}^{i},\xi^{i+1},\boldsymbol{\phi}^{i+1},\boldsymbol{\kappa}^{i})\\
&=f(\mathbf{x}^{i+1})+\frac{\varphi}{2}\|\mathbf{x}^{i+1}-\xi^{i+1}e^{j\boldsymbol{\phi}^{i+1}}+\boldsymbol{\kappa}^{i}\|^2\\
&\quad-f(\mathbf{x}^{i})-\frac{\varphi}{2}\|\mathbf{x}^{i}-\xi^{i+1}e^{j\boldsymbol{\phi}^{i+1}}+\boldsymbol{\kappa}^{i}\|^2\\
&\overset{(a)}{=}f(\mathbf{x}^{i+1})-f(\mathbf{x}^{i})-\frac{\varphi}{2}\|\mathbf{x}^{i+1}-\mathbf{x}^{i}\|^2\\
&\quad-\varphi\mathrm{Re}\left[\left(\mathbf{x}^{i+1}-\xi^{i+1}e^{j\boldsymbol{\phi}^{i+1}}+\boldsymbol{\kappa}^{i}\right)^H\left(\mathbf{x}^{i}-\mathbf{x}^{i+1}\right)\right]\\
&\overset{(b)}{=}f(\mathbf{x}^{i+1})-f(\mathbf{x}^{i})-\frac{\varphi}{2}\|\mathbf{x}^{i+1}-\mathbf{x}^{i}\|^2\\
&\quad+\mathrm{Re}\left[\left(\nabla f(\mathbf{x}^{i+1})\right)^H\left(\mathbf{x}^{i}-\mathbf{x}^{i+1}\right)\right]\\
&\overset{(c)}{\leq}-\frac{\varphi}{2}\|\mathbf{x}^{i+1}-\mathbf{x}^{i}\|^2.
\end{aligned}\tag{86}$$

where in (a) we used the cosine rule: $\|b+c\|^2-\|a+c\|^2=\|b-a\|^2+2\langle a+c,b-a\rangle$ with $a=\mathbf{x}^{i+1},b=\mathbf{x}^{i},c=-\xi^{i+1}e^{j\boldsymbol{\phi}^{i+1}}+\boldsymbol{\kappa}^{i}$; in (b) we used (81); in (c) we used the fact that $f(\mathbf{x})$ is convex.

Combining (83)–(86) yields

$$\begin{aligned}
&L_\varphi(\mathbf{x}^{i+1},\xi^{i+1},\boldsymbol{\phi}^{i+1},\boldsymbol{\kappa}^{i+1})-L_\varphi(\mathbf{x}^{i},\xi^{i},\boldsymbol{\phi}^{i},\boldsymbol{\kappa}^{i})\\
&\leq\left(\frac{4\|\sum_{p=1}^{P}\mathbf{A}_p\mathbf{A}_p^H\|_F^2}{\varphi}-\frac{\varphi}{2}\right)\|\mathbf{x}^{i+1}-\mathbf{x}^{i}\|^2,
\end{aligned}\tag{87}$$

which implies that if $\varphi>2\sqrt{2}\|\sum_{p=1}^{P}\mathbf{A}_p\mathbf{A}_p^H\|_F$, the value of the augmented Lagrangian function $L_\varphi(\mathbf{x},\xi,\boldsymbol{\phi},\boldsymbol{\kappa})$ will always decrease as the iterative process goes on.

Part 3. Since the augmented Lagrangian function can be rewritten as

$$\begin{aligned}
&L_\varphi(\mathbf{x}^{i+1},\xi^{i+1},\boldsymbol{\phi}^{i+1},\boldsymbol{\kappa}^{i+1})\\
&=f(\mathbf{x}^{i+1})+\mathrm{Re}\left[\left(\boldsymbol{\kappa}^{i+1}\right)^H\left(\mathbf{x}^{i+1}-\xi^{i+1}e^{j\boldsymbol{\phi}^{i+1}}\right)\right]\\
&\quad+\frac{\varphi}{2}\|\mathbf{x}^{i+1}-\xi^{i+1}e^{j\boldsymbol{\phi}^{i+1}}\|^2\\
&\overset{(a)}{=}f(\mathbf{x}^{i+1})+\mathrm{Re}\left[\left(\nabla f(\mathbf{x}^{i+1})\right)^H\left(\xi^{i+1}e^{j\boldsymbol{\phi}^{i+1}}-\mathbf{x}^{i+1}\right)\right]\\
&\quad+\frac{\varphi}{2}\|\mathbf{x}^{i+1}-\xi^{i+1}e^{j\boldsymbol{\phi}^{i+1}}\|^2\\
&\overset{(b)}{\geq}f(\xi^{i+1}e^{j\boldsymbol{\phi}^{i+1}}),
\end{aligned}\tag{88}$$

where in (a) we used (81); in (b) we used the Lipschitz continuity of the gradient of $f(\mathbf{x})$ [32]. In addition, combining $f(\mathbf{x})\geq 0$ with (88) it is easily found that Part 3 is true.

According to Parts 2–3 and $\varphi>2\sqrt{2}\|\sum_{p=1}^{P}\mathbf{A}_p\mathbf{A}_p^H\|_F$, we have

$$\lim_{i\to\infty}\|\mathbf{x}^{i+1}-\mathbf{x}^{i}\|=0,\tag{89}$$

by (82) we further have

$$\lim_{i\to\infty}\|\boldsymbol{\kappa}^{i+1}-\boldsymbol{\kappa}^{i}\|=0.\tag{90}$$

From the dual update step in (49c), $\lim_{i\to\infty}\|\boldsymbol{\kappa}^{i+1}-\boldsymbol{\kappa}^{i}\|=0$ implies that

$$\lim_{i\to\infty}\|\mathbf{x}^{i}-\xi^{i}e^{j\boldsymbol{\phi}^{i}}\|=0,\tag{91}$$

thus, Part 4 holds.

Using the fact that $\lim_{i\to\infty}\mathbf{x}^{i}=\mathbf{x}^{\star}$ and $\lim_{i\to\infty}\xi^{i}e^{j\boldsymbol{\phi}^{i}}=\xi^{\star}e^{j\boldsymbol{\phi}^{\star}}$, from (91), we have

$$\mathbf{x}^{\star}=\xi^{\star}e^{j\boldsymbol{\phi}^{\star}}.\tag{92}$$

By Eq. (79), and the fact that $\lim_{i\to\infty}\boldsymbol{\kappa}^{i}=\boldsymbol{\kappa}^{\star}$, we get

$$\mathbf{0}\in\nabla f(\mathbf{x}^{\star})+\varphi\boldsymbol{\kappa}^{\star},\tag{93}$$

and thus Part 5 holds.

The proof is complete. ■

REFERENCES

[1] J. Li and P. Stoica, "MIMO radar with colocated antennas," *IEEE Signal Process. Mag.*, vol. 24, no. 5, pp. 106–114, Sep. 2007.

[2] P. Stoica, J. Li, and Y. Xie, "On probing signal design for MIMO radar," *IEEE Trans. Signal Process.*, vol. 55, no. 8, pp. 4151–4161, Aug. 2007.

[3] J. Li and P. Stoica, *MIMO Radar Signal Processing*. New York, NY, USA: Wiley, 2008.

[4] H. Li, Z. Wang, J. Liu, and B. Himed, "Moving target detection in distributed MIMO radar on moving platforms," *IEEE J. Sel. Topics Signal Process.*, vol. 9, no. 8, pp. 1524–1535, Dec. 2015.

[5] C. A. Balanis, *Antenna Theory: Analysis and Design*. New York, NY, USA: Wiley, 2005.

[6] D. R. Fuhrmann and G. S. Antonio, "Transmit beamforming for MIMO radar systems using signal cross-correlation," *IEEE Trans. Aerosp. Electron. Syst.*, vol. 44, no. 1, pp. 171–186, Jan. 2008.

[7] H. Li and B. Himed, "Transmit subaperturing for MIMO radars with co-located antennas," *IEEE J. Sel. Topics Signal Process.*, vol. 4, no. 1, pp. 55–65, Feb. 2010.

[8] S. M. Karbasi, A. Aubry, A. D. Maio, and M. H. Bastani, "Robust transmit code and receive filter design for extended targets in clutter," *IEEE Trans. Signal Process.*, vol. 63, no. 8, pp. 1965–1976, Apr. 2015.
[9] G. Cui, H. Li, and M. Rangaswamy, "MIMO radar waveform design with constant modulus and similarity constraints," *IEEE Trans. Signal Process.*, vol. 62, no. 2, pp. 343–353, Jan. 2014.
[10] S. Ahmed, J. S. Thompson, Y. R. Petillot, and B. Mulgrew, "Unconstrained synthesis of covariance matrix for MIMO radar transmit beampattern," *IEEE Trans. Signal Process.*, vol. 59, no. 8, pp. 3837–3849, Aug. 2011.
[11] J. Lipor, S. Ahmed, and M. S. Alouini, "Fourier-based transmit beampattern design using MIMO radar," *IEEE Trans. Signal Process.*, vol. 62, no. 9, pp. 2226–2235, May 2014.
[12] G. Hua and S. S. Abeysekera, "MIMO radar transmit beampattern design with ripple and transition band control," *IEEE Trans. Signal Process.*, vol. 61, no. 11, pp. 2963–2974, Jun. 2013.
[13] S. Ahmed and M. Alouini, "A survey of correlated waveform design for multifunction software radar," *IEEE Aerosp. Electron. Syst. Mag.*, vol. 31, no. 3, pp. 19–31, Mar. 2016.
[14] P. Stoica, J. Li, and X. Zhu, "Waveform synthesis for diversity-based transmit beampattern design," *IEEE Trans. Signal Process.*, vol. 56, no. 6, pp. 2593–2598, Jun. 2008.
[15] S. Jardak, S. Ahmed, and M. S. Alouini, "Generation of correlated finite alphabet waveforms using Gaussian random variables," *IEEE Trans. Signal Process.*, vol. 62, no. 17, pp. 4587–4596, Sep. 2014.
[16] D. R. Fuhrmann and G. S. Antonio, "Transmit beamforming for MIMO radar systems using partial signal correlation," in *Conf. Rec. 38th Asilomar Conf. Signals, Syst. Comput.*, Nov. 2004, vol. 1, pp. 295–299.
[17] N. Shariati, D. Zachariah, and M. Bengtsson, "Minimum sidelobe beampattern design for MIMO radar systems: A robust approach," in *Proc. IEEE Int. Conf. Acoust., Speech Signal Process.*, May 2014, pp. 5312–5316.
[18] A. Aubry, A. D. Maio, and Y. Huang, "MIMO radar beampattern design via PSL/ISL optimization," *IEEE Trans. Signal Process.*, vol. 64, no. 15, pp. 3955–3967, Aug. 2016.
[19] S. Ahmed and M. S. Alouini, "MIMO radar transmit beampattern design without synthesising the covariance matrix," *IEEE Trans. Signal Process.*, vol. 62, no. 9, pp. 2278–2289, May 2014.
[20] X. Zhang, Z. He, L. Rayman-Bacchus, and J. Yan, "MIMO radar transmit beampattern matching design," *IEEE Trans. Signal Process.*, vol. 63, no. 8, pp. 2049–2056, Apr. 2015.
[21] S. Ahmed and M. S. Alouini, "MIMO-radar waveform covariance matrix for high SINR and low side-lobe levels," *IEEE Trans. Signal Process.*, vol. 62, no. 8, pp. 2056–2065, Apr. 2014.
[22] Z. F. Cheng, Y. B. Zhao, H. Li, and P. L. Shui, "Sparse representation framework for MIMO radar transmit beampattern matching design," *IEEE Trans. Aerosp. Electron. Syst.*, vol. 53, no. 1, pp. 520–529, Feb. 2017.
[23] H. He, J. Li, and P. Stoica, *Waveform Design for Active Sensing Systems: A Computational Approach*. Cambridge, U.K: Cambridge Univ. Press, 2012.
[24] J. Liang, H. C. So, J. Li, and A. Farina, "Unimodular sequence design based on alternating direction method of multipliers," *IEEE Trans. Signal Process.*, vol. 64, no. 20, pp. 5367–5381, Oct. 2016.
[25] J. Liang, H. C. So, C. S. Leung, J. Li, and A. Farina, "Waveform design with unit modulus and spectral shape constraints via lagrange programming neural network," *IEEE J. Sel. Topics Signal Process.*, vol. 9, no. 8, pp. 1377–1386, Dec. 2015.
[26] S. Imani, M. M. Nayebi, and S. Ghorashi, "Transmit signal design in co-located MIMO radar without covariance matrix optimization," *IEEE Trans. Aerosp. Electron. Syst.*, vol. 53, no. 5, pp. 2178–2186, Oct. 2017.
[27] O. Aldayel, V. Monga, and M. Rangaswamy, "Tractable transmit MIMO beampattern design under a constant modulus constraint," *IEEE Trans. Signal Process.*, vol. 65, no. 10, pp. 2588–2599, May 2017.
[28] Z. Cheng, Z. He, S. Zhang, and J. Li, "Constant modulus waveform design for MIMO radar transmit beampattern," *IEEE Trans. Signal Process.*, vol. 65, no. 18, pp. 4912–4923, Sep. 2017.
[29] S. Boyd, N. Parikh, E. Chu, B. Peleato, and J. Eckstein, "Distributed optimization and statistical learning via the alternating direction method of multipliers," *Found. Trends Mach. Learn.*, vol. 3, no. 1, pp. 1–122, 2011.
[30] Z. Wen, C. Yang, X. Liu, and S. Marchesini, "Alternating direction methods for classical and ptychographic phase retrieval," *Inverse Problems*, vol. 28, no. 11, Nov. 2012, Art. no. 115010.
[31] M. Hong and Z.-Q. Luo, "On the linear convergence of the alternating direction method of multipliers," *Math. Program.*, vol. 162, no. 1, pp. 165–199, Mar. 2017.
[32] M. Hong, Z.-Q. Luo, and M. Razaviyayn, "Convergence analysis of alternating direction method of multipliers for a family of nonconvex problems," *SIAM J. Optim.*, vol. 26, no. 1, pp. 337–364, 2016.
[33] Y. Wang, W. Yin, and J. Zeng, "Global convergence of ADMM in nonconvex nonsmooth optimization," *J. Scientific Comput.*, Jun. 2018.
[34] A. Aubry, A. D. Maio, and M. M. Naghsh, "Optimizing radar waveform and Doppler filter bank via generalized fractional programming," *IEEE J. Sel. Topics Signal Process.*, vol. 9, no. 8, pp. 1387–1399, Dec. 2015.
[35] Y. Huang and D. P. Palomar, "Randomized algorithms for optimal solutions of double-sided QCQP with applications in signal processing," *IEEE Trans. Signal Process.*, vol. 62, no. 5, pp. 1093–1108, Mar. 2014.
[36] M. Soltanalian and P. Stoica, "Designing unimodular codes via quadratic optimization," *IEEE Trans. Signal Process.*, vol. 62, no. 5, pp. 1221–1234, Mar. 2014.
[37] G. Cui, X. Yu, G. Foglia, Y. Huang, and J. Li, "Quadratic optimization with similarity constraint for unimodular sequence synthesis," *IEEE Trans. Signal Process.*, vol. 65, no. 18, pp. 4756–4769, Sep. 2017.
[38] A. Aubry, V. Carotenuto, A. D. Maio, A. Farina, and L. Pallotta, "Optimization theory-based radar waveform design for spectrally dense environments," *IEEE Aerosp. Electron. Syst. Mag.*, vol. 31, no. 12, pp. 14–25, Dec. 2016.
[39] A. D. Maio, Y. Huang, M. Piezzo, S. Zhang, and A. Farina, "Design of optimized radar codes with a peak to average power ratio constraint," *IEEE Trans. Signal Process.*, vol. 59, no. 6, pp. 2683–2697, Jun. 2011.
[40] J. Liu, A. B. Gershman, Z.-Q. Luo, and K. M. Wong, "Adaptive beamforming with sidelobe control: A second-order cone programming approach," *IEEE Signal Process. Lett.*, vol. 10, no. 11, pp. 331–334, Nov. 2003.
[41] S. Boyd and L. Vandenberghe, *Convex Optimization*. Cambridge, U.K.: Cambridge Univ. Press, 2004.
[42] G. H. Golub and C. F. Van Loan, *Matrix Computations*, vol. 3. Baltimore, MD, USA: JHU Press, 2012.
[43] J. A. Tropp, I. S. Dhillon, R. W. Heath, and T. Strohmer, "Designing structured tight frames via an alternating projection method," *IEEE Trans. Inf. Theory*, vol. 51, no. 1, pp. 188–209, Jan. 2005.

Wen Fan was born in China. He is currently working toward the Ph.D. degree at School of Electronics and Information, Northwestern Polytechnical University, Xi'an, China.

His current research interests include array signal processing, image processing, and their applications.

Junli Liang (SM'16) was born in China. He received the Ph.D. degree in signal and information processing from the Institute of Acoustics, Chinese Academy of Sciences, Beijing, China. He is currently a Professor with the School of Electronics and Information, Northwestern Polytechnical University, Xi'an, China. His research interests include radar signal processing, image processing, and their applications.

Jian Li (S'87–M'91–SM'97–F'05) received the M.Sc. and Ph.D. degrees in electrical engineering from The Ohio State University, Columbus, OH, USA, in 1987 and 1991, respectively. From April 1991 to June 1991, she was an Adjunct Assistant Professor with the Department of Electrical Engineering, The Ohio State University. From July 1991 to June 1993, she was an Assistant Professor with the Department of Electrical Engineering, University of Kentucky, Lexington, Kentucky. Since August 1993, she has been with the Department of Electrical and Computer Engineering, University of Florida, Gainesville, where she is currently a Professor. In Fall 2007, she was on sabbatical leave at MIT, Cambridge, MA, USA. Her current research interests include spectral estimation, statistical and array signal processing, and their applications. For more detail about biography, please see the web: http://www.sal.ufl.edu/li.html.